

Application of a Hybrid ARIMA-LSTM Model Based on The SPEI For Drought Forecasting

Dehe Xu

North China University of Water Resources and Electric Power

Qi Zhang (✉ 895300576@qq.com)

North China University of Water Resources and Electric Power

Yan Ding

North China University of Water Resources and Electric Power

De Zhang

State Key Laboratory of Geo-Information Engineering

Research Article

Keywords: Drought forecasting, SPEI, ARIMA-SVR, LS-SVR, ARIMA-LSTM

Posted Date: May 10th, 2021

DOI: <https://doi.org/10.21203/rs.3.rs-301080/v1>

License: © ⓘ This work is licensed under a Creative Commons Attribution 4.0 International License.

[Read Full License](#)

Version of Record: A version of this preprint was published at Environmental Science and Pollution Research on August 17th, 2021. See the published version at <https://doi.org/10.1007/s11356-021-15325-z>.

21 SPEI1 are 0.043,0.168 and 0.368, respectively, and the NSEs of SPEI24 is 0.781, 0.543
22 and 0.93, respectively. This finding indicates that when the lead time remains
23 unchanged, the prediction accuracy of the hybrid ARIMA-SVR, LS-SVR and ARIMA-
24 LSTM models for the SPEI at various scales is gradually improved with increasing time
25 scale, and the prediction accuracy of the model with a one-month lead time is higher
26 than that of the model with a two-month lead time. In addition, the ARIMA-LSTM
27 model has the highest prediction accuracy at the 6-, 12-, and 24-month scales, indicating
28 that the model is more suitable for the forecasting of long-term drought in China.

29

30 *Keywords:* Drought forecasting; SPEI; ARIMA-SVR; LS-SVR; ARIMA-LSTM

31

32 1. Introduction

33 From a global perspective, drought is one of the most serious natural disasters in
34 the world, with the widest impact and incurring greatest economic losses (Tian et al.
35 2018). In recent years, global warming, excessive carbon emissions and other issues
36 have led to the continued increase of agricultural droughts, which seriously threatens
37 China's domestic and global food production, and accurate assessment, monitoring
38 and analysis of drought has been a hot topic of domestic and foreign scholars.
39 Therefore, quantitative research on drought is conducive to improving drought
40 monitoring, strengthening the development of drought prediction, and identifying
41 strategies. Generally, easy-to-calculate drought indicators are used to monitor and
42 evaluate the drought intensity, duration and disaster area (Zhang et al. 2019). Due to
43 the wide application range and variety of drought indicators and the different
44 understanding of drought in different majors and disciplines, a variety of drought
45 indicators have been proposed (Yao et al. 2018a).

46 Common drought indices include the meteorological-related Palmer drought
47 severity index (PDSI) (Paulo et al. 2012; Vicente-Serrano et al. 2015; Dai et al. 2004),
48 SPI (Mckee et al. 1993) and SPEI (Vicente-Serrano et al. 2010), the soil water
49 content-related soil moisture anomaly index (SMAI) (Gao et al. 2016) and
50 evapotranspiration deficit index (ETDI) (Narasimhan and Srinivasan 2005) and the
51 hydrological-related Palmer hydrological drought index (PHDI) (Tatli and Türkeş
52 2011) and standardized water-level index (SWI) (Bhuiyan et al. 2006). In addition, the

53 remote sensing-based normalized differential vegetation index (NDVI) (Gu et al.
54 2007) is also frequently used. Both the PDSI and SPEI require temperature and
55 precipitation data, and the SMAI and ETDI are more complicated to calculate than the
56 SPI. The SWI only considers groundwater, the NDVI requires long-term data, and
57 satellite data have no long-term history. SPI is multi-scale and computationally simple
58 because rainfall is the only input data (Chen and Sun 2015; Wang et al. 2015, 2016).
59 The SPEI is based on the SPI but adds a temperature component that allows the SPEI
60 to account for the effect of temperature on the development of drought through basic
61 water balance calculations (Soh et al. 2018; Yao et al. 2018b). Li et al. (2020)
62 elucidated drought characteristics of China during 1980-2015 using two commonly
63 used meteorological drought indices: SPI and SPEI. Given the fact that potential
64 evapotranspiration increases in a warming climate, Li et al. (2020) show that SPEI
65 may be more suitable than SPI in monitoring drought under climate change.
66 Therefore, the SPEI were chosen to monitor drought in this study.

67 In recent years, data-driven models have been commonly used for drought
68 forecasting (Adamowski 2008; Mossad and Alazba 2015; Karthika et al. 2017; Rafiei-
69 Sardooi et al. 2018; Fung et al. 2019b). There are many models used to forecast
70 drought, such as the ARIMA model (Mishra and Desai 2005, 2006; Mishra et al.
71 2007; Han et al. 2010), which is the most widely adopted stochastic approach. Tian et
72 al. (2016) used the ARIMA model to predict the agricultural drought in the
73 Guanzhong Plain, mainly on the time series of the VTCI drought monitoring results;

74 the results showed that the absolute error of the AR(1) model was lower than that of
75 the SARIMA model, both in frequency distribution and statistical results. It shows
76 that the ARIMA model can better predict the type and extent of drought and can be
77 used for drought prediction in the plains. However, the author did not conduct the
78 analysis and prediction from multiple time scales, so the results obtained were limited
79 and the model was not necessarily applicable to all time scales. Mossad and Alazba
80 (2015) developed several ARIMA models for drought forecasting using multiscale
81 SPEI in hyperarid climates, and showed that ARIMA models can be very useful tools
82 for drought forecasting that can help water resource managers and planners to take
83 precautions considering the severity of drought in advance. However, stochastic
84 models are linear models with limited ability to predict nonlinear data; therefore,
85 when the time scale is large, ARIMA models cannot perform well at all scales. In
86 recent years, ANN models have been used by researchers to improve the prediction
87 accuracy of nonlinear data, as traditional data-driven models do not predict nonlinear
88 data well(Ochoa-Rivera 2008; Marj and Meijerink 2011; Sigaroodi et al. 2013;
89 Kousari et al. 2017; Seibert et al. 2017). ANNs have been used as drought prediction
90 tools in many studies (Belayneh and Adamowski 2012; Deo and Şahin 2015;
91 Belayneh et al. 2016; Borji et al. 2016; Chen et al. 2017; Seibert et al. 2017) and have
92 achieved good results. There are many kinds of ANNs, including recurrent neural
93 networks (RNNs) and LSTM networks (Poornima and Pushpalatha 2019). RNNs and
94 traditional ANNs have been compared in terms of time series model prediction, and it

95 has been found that RNNs achieve a higher prediction accuracy than traditional
96 ANNs. RNNs have shown significant effects on the forecasting of data sequences.
97 However, when the sequence length is too large, there is a dramatic increase in the
98 training time of the RNN. Based on the above problems, the LSTM network
99 (Hochreiter 1997) is proposed, which improves the hidden layer of the RNN, expands
100 the memory function of the network, enables the model to obtain more persistent
101 information, and slows down the information decay rate (Tran Anh et al. 2019).
102 LSTM is a kind of deep learning method and has made great progress in time series
103 prediction (Zhang et al. 2018; Jeong and Park 2019; Qi et al. 2019; Tran Anh et al.
104 2019). However, it is difficult to use LSTM architecture in short-term time series
105 prediction or with meteorological drought indices. Poornima et al. (2019) used LSTM
106 to predict the multitime scale SPI and SPEI and found that the model could better
107 process real-time nonlinear data and achieve good the long-term prediction. However,
108 because the prediction accuracy is not high or cannot improve the short-term
109 prediction accuracy, a variety of hybrid models are used to predict the drought index.
110 Modaresi et al. (2018) used four data-driven models to forecast the monthly inflow to
111 the K dam, and a cross-validation approach was used to determine the optimal values
112 of the model parameters. The results show that the LS-SVR model performs best
113 under nonlinear conditions and the ANN performs best under linear conditions. Xu et
114 al. (2020) used the ARIMA model and hybrid ARIMA-SVR model, for predicting the
115 SPEI with a lead time of one month. By applying the mean absolute error (MAE), root

116 mean square error (RMSE), NSE and coefficient of determination as model evaluation
117 metrics, it was found that the ARIMA-SVR model was superior with the trend in
118 improving accuracy when the timescale of the SPI increased. Therefore this paper
119 uses ARIMA-LSTM, LS-SVR and ARIMA-SVR models for comparison of
120 prediction accuracy.

121 The objective of this paper is to propose a hybrid model with the advantages of a
122 linear and nonlinear models to improve the short-term prediction accuracy. The aim of
123 this paper is to use the 6 models to predict the multiscale SPEI computed from 613
124 sites in China, and to explore the prediction accuracy of different models at each scale
125 with the help of evaluation and validation metrics. Because the kriging interpolation
126 method is commonly used in drought index analyses (Manatsa et al. 2008; Karavitis et
127 al. 2012; Afzali et al. 2016; Jain and Flannigan 2017; Cai et al. 2019), this paper will
128 describe the use of the improved kriging interpolation method, empirical Bayesian
129 kriging (EBK), in ArcGIS to conduct a visual analysis of SPEI12 observed values and
130 fitted values of the three hybrid models from 2014 and 2015. The performance of all
131 the models is compared using measures of persistence, namely, the mean squared
132 error (MSE), NSE, RMSE and MAE.

133

134 2. Material and methods

135 2.1 Study area and data

136 China has a descending 3-terrace-topography from the west to the east with
137 much diversified topography (Fig 1). Considering the multi-year average temperature,
138 precipitation and moisture conditions, China is divided into seven natural sub-regions
139 (Yao et al. 2018b), which include the temperate and warm-temperate desert of
140 northwest China (sub-region 1), the temperate grassland of Inner Mongolia (sub-
141 region 2), the temperate humid and sub-humid northeast China (sub-region 3), the
142 warm-temperate humid and sub-humid north China (sub-region 4), the subtropical
143 humid central and south China (sub-region 5), the Qinghai-Tibetan Plateau (sub-
144 region 6), and the tropic humid south China (sub-region 7). The original data were
145 derived from the National Meteorological Information Center (<http://data.cma.cn>).

146 2.2 Methods

147 2.2.1 SPEI

148 In 2009, the World Meteorological Organization (WMO) recommended the
149 SPEI as the main meteorological drought indices, which countries can use to monitor
150 and track drought conditions (Hayes et al. 1996). By defining the SPEI as widely used
151 indices, the WMO provides guidance to countries seeking to establish early warning
152 levels for droughts. The probability density function (PDF) that has been used for the
153 SPEI is the log-logistic function, as suggested by Mckee et al. (1993) and Vicente-
154 Serrano et al. (2010), respectively. Since both Yao et al. (2018b) and Li et al. (2020)
155 used the SPEI to monitor the drought situation in China, the log-logistic PDFs are
156 available for meteorological sites in China.

157 The Penman-Monteith (PM) method has been adopted by the International
 158 Commission on Irrigation and Drainage (ICID) as the standard procedure for
 159 computing PET(Yao et al. 2018b). SPEI is calculated using precipitation and PET
 160 series for each station, each subregion. The computation procedure of SPEI follows:

$$161 \quad a = 1 + \left(\frac{\alpha}{x - \gamma}\right)^\beta \quad (1)$$

$$162 \quad F(x) = [a]^{-1} \quad (2)$$

163 P is the probability of a definite D value:

$$164 \quad P = 1 - F(x) \quad (3)$$

165 For $P \leq 0.5$,

$$166 \quad w = \sqrt{-2\ln(P)} \quad (4)$$

$$167 \quad SPEI = W - \frac{(c_2W + c_1)W + c_0}{[(d_3W + d_2)W + d_1]W + 1} \quad (5)$$

168 For $P > 0.5$,

$$169 \quad w = \sqrt{-2\ln(1 - P)} \quad (6)$$

$$170 \quad SPEI = -(W - \frac{(c_2W + c_1)W + c_0}{[(d_3W + d_2)W + d_1]W + 1}) \quad (7)$$

171 Where $c_0=2.515517$, $c_1=0.802853$, $c_2=0.010328$, $d_1=1.432788$, $d_2=0.189269$,

172 $d_3=0.001308$. The classification of dry and wet spells resulting from the values of

173 the SPEI is shown in Table 1.

174

175 2.2.2 ARIMA modeling steps

176 ARIMA is a linear model that has been widely used in drought prediction in recent

177 years (Kisi et al. 2015; Choubin and Malekian 2017). The formula for ARIMA and

178 the model ordering process can be found in detail in Xu et al. (2020). ARIMA models

179 were developed based on the Box and Jenkins approach. The formula for a general
180 non-seasonal ARIMA model can be abbreviated as follows(Xu et al. 2020):

$$181 \quad Z_t = \frac{\theta(B)\alpha_t}{\phi(B)\nabla^d} \quad (8)$$

$$182 \quad \phi B = (1 - \phi_1 B - \phi_2 B^2 - \dots - \phi_p B^p) \quad (9)$$

183 And

$$184 \quad \theta B = (1 - \theta_1 B - \theta_2 B^2 - \dots - \theta_q B^q) \quad (10)$$

185 where Z_t is the observed time series and B is a back shift operator. ϕB and θB are
186 polynomials of order p and q , respectively. ∇^d describes the differencing operation
187 to data series to make the data series stationary and d is the number of regular
188 differencing.

189 In this paper, ACF and PACF (Fig.6) are used to order the model, and AIC, BIC
190 and HQIC parametrics were combined to select the optimal model parameters.
191 Finally, 80% of the data were selected as the training set and 20% as the test set using
192 a cross-validation approach. The results of the SPEI with one month of lead time are
193 shown in Fig. 8 and Fig. 9, respectively, and the results of the one-to-two-month lead
194 time are shown in Table 4 and Table 5.

195

196 2.2.3 LS-SVR model

197 Support vector machine regression is a support vector machine algorithm used to
198 solve regression problems, which is an extension and application of support vector
199 machines to regression estimation problems. If we extend the conclusions obtained by

200 the support vector machine for classification problems to the regression function, it
201 becomes support vector regression, which is commonly used for time series
202 prediction, nonlinear modeling and prediction, and optimization control(Modaresi et
203 al. 2018). Details and formulas about the SVR can be seen in the article by Xu et al.
204 (2020).

205 LS-SVMR, or least-squares support vector regression, was proposed by J.A.K
206 Suykens (Suykens et al. 2002) as an improvement to the SVM to facilitate its solution.
207 Compared with the standard SVM, LS-SVMR replaces the inequality constraint in the
208 SVM with an equation constraint, and the solution process becomes a set of equation
209 equations, which avoids the time-consuming quadratic planning problem of solution
210 and speeds up the solution process relatively fast. Details and formulas about the SVR
211 can be seen in the article by Suykens et al. (2002).

212 The LS-SVR modeling steps are as follows:

213 First of all, the data is standardized processing, because this article was used radial
214 basis function (RBF), so to calculate the distance of two points in high-dimensional
215 space, it is necessary to standardize the data first, in order to avoid the effect of the
216 scale on the calculation distance. Secondly, set the parameters sigma and gama, where
217 sigma represents the degree of dispersion of the point distribution in high-dimensional
218 space, gama balances the two items of the target function, and this paper uses cross-
219 validation to give the appropriate sigma value and gama value.

220

221 2.2.4 LSTM model

222 LSTM is a variant of the RNN network. Compared to traditional RNNs, its hidden
223 layer module structure has been greatly redesigned. Although RNNs can effectively
224 handle nonlinear time series, there are still two problems: (1) Due to gradient
225 vanishing and gradient explosion, RNNs cannot handle time series with excessive
226 delays; (2) training the RNN model requires a predetermined delay window length,
227 but it is difficult to automatically obtain the optimal value of this parameter. Thus, the
228 LSTM model emerged. The LSTM model replaces the hidden layer of RNN cells with
229 LSTM cells to achieve long-term memory. The special design of the LSTM model
230 makes it able to learn long-term dependencies and is particularly suitable for time
231 series analyses.

232 The hidden layer of the LSTM module is also called a memory module. The
233 specific structure is shown in Fig. 2. For the sake of understanding, memory modules
234 are often compared to computer memory. The memory module consists of a storage
235 unit and three computing components. The three computing components are called
236 input gates, output gates, and forget gates, which control the reading, writing, and
237 resetting of memory cell data, respectively. As seen from the figure, LSTM is a four-
238 layer structure, and each structure is connected to and interacts with the others. The
239 yellow part of the figure shows the various activation functions inside the memory
240 module, and the red part represents the basic operation of the vector, for example,
241 vector addition and product operations. The arrows represent the direction in which

242 the vector is transmitted in the network. The confluence of two solid lines in the
 243 figure indicates the vector combination of two parts. A solid line is divided into
 244 multiple lines to indicate that the vector is copied and then flows to different parts of
 245 the network.

246 The calculation of the LSTM hidden layer is shown in Fig. 3, and its forward
 247 calculation method can be expressed as:

$$248 \quad i_t = \sigma(W_i x_t + U_i h_{t-1} + b_i) \quad (11)$$

$$249 \quad f_t = \sigma(W_f x_t + U_f h_{t-1} + b_f) \quad (12)$$

$$250 \quad C_t = f_t \otimes C_{t-1} + i_t \otimes \tilde{C}_t \quad (13)$$

$$251 \quad \tilde{C}_t = \tanh(W_c x_t + U_c h_{t-1} + b_c) \quad (14)$$

$$252 \quad o_t = \sigma(W_o x_t + U_o h_{t-1} + b_o) \quad (15)$$

$$253 \quad h_t = o_t \otimes \tanh(C_t) \quad (16)$$

254 where i , f , C and o denote the input gate, forget gate, the cell state vector and
 255 output gate, respectively. W denotes the matrix of weights, b denotes the bias
 256 vectors, and U denotes the matrix of weights to the hidden; σ and \tanh are sigmoid
 257 and hyperbolic tangent activation functions, respectively. The elementwise
 258 multiplication of two vectors is denoted by \otimes .

259 In this paper, multitime scale SPEI values were used in the prediction because
 260 the data are a time series related to the previous sequence value. Since the number of
 261 hidden layers determines the model's fitting ability, to prevent overfitting, this paper

262 proposes an early stopping technique, which stops training when the loss function no
263 longer drops. The loss function is defined below:

$$264 \quad LOSS = \sum_{i=1}^N (y_i - \hat{y}_i)^2 \quad (17)$$

265 where y_i is the measured value at time i and \hat{y}_i is the predicted value at time i .

266 The LSTM modeling steps are as follows:

267 1) Preprocessing of the input data

268 The original time series should not be directly input into the model as input data.

269 To obtain better training results, the original time series needs to be preprocessed.

270 Usually, the data processed by a neural network model are normalized data because

271 the training effect of the model is affected by the amount of original data. The

272 normalized data limit the data to a range of $[-1, 1]$, which can eliminate the impact on

273 the neural network due to differences in the dimensions of each dataset, facilitate the

274 analysis of data, and improve the training speed of the model.

275 2) Model construction

276 The LSTM network in this paper was built based on the Keras framework of the

277 Python 3.7 platform. Therefore, before modeling the training data, the methods and

278 parameters need to be configured in the LSTM model based on the Keras framework.

279 The hidden layer of the LSTM in this paper was composed of 20 storage units, the

280 number of iterations was 300, the batch size was set to 1, the activation function was

281 set to ReLU, the loss function was the MSE, and the optimizer was SGD. However,

282 the number of hidden layers directly determines the quality of the model's fitting

283 ability. To avoid overfitting, the MSE is adopted to describe and select the
284 performance of the model corresponding to the number of hidden layers of the LSTM
285 network.

286 3) Fitting model and parameter tuning

287 The golden section method was used in this paper to select the optimal number of
288 hidden neurons. The golden section method involves first finding the ideal number of
289 hidden layer nodes in the interval [a, b], expanding the search interval according to
290 the golden section principle, that is, obtaining the interval [b, c] (where $b=0.619*(ca)+$
291 a), and searching for the best value in [b, c]. The batch size is the number of samples
292 of model weight updates. The weight was updated after each sample. Therefore, the
293 batch size was set to 1, and the process is called random gradient descent. Common
294 activation functions are sigmoid, tanh, and ReLU. Because the time-based back
295 propagation algorithm was used for network training, the sigmoid function is prone to
296 gradient vanishing during backpropagation and was unable to complete deep network
297 training, the SGD obtained by ReLU converged much faster than that obtained by the
298 sigmoid and tanh activation functions, so ReLU was used as the activation function in
299 this paper. The number of iterations was set as high as possible. The early stopping
300 method was used in this article to prevent overfitting. Since the number of training
301 cycles made the process very time-consuming, the loss function is set to check the
302 performance of the model on the training and verification dataset. Once overlearning
303 starts, training stops, so early stopping was used to suppress overfitting; that is, after

304 each epoch, the test results were obtained on the verification set. When the error
305 increases, the training was stopped, and the weight after stopping was taken as the
306 final parameter of the network.

307 4) Training output and anti-normalization

308 The training data were programmed into the network training model, and when
309 the number of iterations exceeded the set threshold, the training ended. The output
310 value of the network was not the final forecast result of the time series. The actual
311 output of the model could be obtained by performing reverse normalization on the
312 output value of the network. Usually, this method is called inverse normalization.

313

314 2.2.5 Hybrid ARIMA-LSTM model

315 In the time series forecasting problem, the characteristics of the linear model and
316 the nonlinear model determine that the former can only recognize the linear pattern of
317 the time series, and the latter has the advantage of being able to mine the nonlinear
318 relationship of the time series. A large number of experiments and applications have
319 shown that using a single model can have a good effect when dealing with a single
320 time series of components (Choubin et al. 2016; Soh et al. 2018; Fung et al. 2019b, a).

321 However, in the face of complex problems, a single model had certain limitations.

322 Because the time series of the research object contains linear components and
323 nonlinear components, a single linear model or a single nonlinear model is not
324 suitable for use.

325 A hybrid model was established using the advantages of both the ARIMA and
 326 LSTM models, as same as hybrid ARIMA-SVR model (Xu et al. 2020a). The
 327 formulas are as follows:

$$328 \quad Y_t = L_t + N_t \quad (18)$$

329 where Y_t is a combination of linear (L_t) and nonlinear parts (N_t).

330 The modeling flow chart is shown in Fig. 4.

331 2.2.5 Evaluation indices

332 In this study, MSE, RMSE, NSE (Nash JE 1970) and MAE were used as indicators
 333 of model evaluation by the following formulas(Belayneh et al. 2016; Deo and Şahin
 334 2016):

$$335 \quad MSE = \frac{SSE}{N} \quad (19)$$

$$336 \quad RMSE = \sqrt{\frac{SSE}{N}} \quad (20)$$

337 where the SSE is the sum of squared errors and N is the number of samples. The SSE
 338 is given by:

$$339 \quad SSE = \sum_{i=1}^N (y_i - \hat{y}_i)^2 \quad (21)$$

340 with the variables already having been defined.

$$341 \quad NSE = 1 - \frac{\sum_{i=1}^N (y_i - \hat{y}_i)^2}{\sum_{i=1}^N (y_i - \bar{y})^2} \quad (22)$$

342 where

$$343 \quad \bar{y} = \frac{\sum_{i=1}^N y_i}{N} \quad (23)$$

344 where y_i is the observed value at time i ($i = 1, \dots, N$), \bar{y} is the mean value taken
345 over N and N is the total data size of y_i , ($i = 1, \dots, N$) and \hat{y}_i is the forecasted value
346 at time i .

347
$$MAE = \frac{1}{N} \sum_{i=1}^N |\hat{y}_i - y_i| \quad (24)$$

348

349 3. Results and discussion

350 3.1 Calculation results of SPEI

351 The matplotlib visualization library in Python 3.6 was used to visualize the
352 multiscale SPEI calculation results, and the calculation steps are shown in section
353 2.2.1 The results of the multiscale SPEI calculations in the 7 regions are shown in
354 Figs. 5. As can be seen from Fig 5, the SPEI of 7 sub-regions in China is on the rise,
355 especially the severity of the drought in sub-region 2, 4, and 6. But on the 12-month
356 scale, the drought in regions 1, 2, and 6 is relatively serious in recent 5 year.

357

358 3.2 ARIMA, SVR and LSTM model predicts results

359 In this paper, the ADF test was conducted in the 7 regions of China, and the P
360 values of the multitime scale SPEI were all less than 0.05 (Table 2), so it was judged
361 that SPEI1, SPEI3, SPEI6, SPEI12 and SPEI24 are stationary time series. The optimal
362 ARIMA parameters of the multiscale SPEI of the 7 sub-regions are selected through
363 the AIC, BIC and HQIC (as shown in Table 3). As the drought situation in sub-
364 region1 is more serious than that in other regions, the sub-region 1 is selected as an

365 example for time series prediction. The prediction results in other regions can be seen
366 in Figs. 10. The results of the one-month lead time of the SPEI are shown in Fig. 8,
367 and the results of the one-to-two-month lead time are shown in Table 4 and Table 5.
368 As seen from Figs. 8, the prediction accuracy of the ARIMA model is the highest for
369 SPEI24 and the lowest for SPEI1. As the time scale increases, the prediction accuracy
370 gradually increases because the ARIMA model is essentially an overall linear
371 autoregressive model that predicts a trend that tends to stabilize as the test set grows
372 (Yurekli et al. 2005; Hu et al. 2007).

373 In this paper, monthly precipitation and temperature data from 613 national
374 meteorological stations from 1980 to 2019 are used to conduct LSTM and SVR
375 modeling with multitime scale SPEI values. Due to the large number of regions, only
376 the same region by the ARIMA model were selected for results presentation for
377 comparative study, and the same dataset predicted by the ARIMA model after cross-
378 validation was also selected. The parameters of the LSTM model are shown in Fig.7.

379 It can be seen from Fig. 8 that the prediction results of the SVR and LSTM models
380 has the lowest accuracy at SPEI1 and the highest accuracy at SPEI24, and the
381 prediction accuracy increases gradually with increasing time scale. And we found that
382 the prediction accuracy of SVR is higher than that of ARIMA model at SPEI1 and
383 SPEI3, but it is lower than that of ARIMA model at SPEI6, SPEI12 and SPEI24. This
384 shows that SVR is more suitable for long-term drought prediction than ARIMA
385 model. LSTM has recently been used in many applications, including drought

386 prediction (Poornima and Pushpalatha 2019), weather prediction (Salman et al. 2018),
387 and water table depth prediction (Zhang et al. 2018), and has achieved good results
388 because it can describe nonlinear relationships. Fig. 7 show that the box diagram of
389 the LSTM model predicting the number of hidden layer neurons of the SPEI at
390 various scales shows that with the increase in the number of hidden layers, the MSE
391 gradually decreases, indicating that the more hidden layers there are, the higher the
392 prediction accuracy of the LSTM. However, to prevent overfitting, this paper adopts a
393 regularization method, namely, the early stopping method (described in section 2.2.3).
394 At present, most studies on LSTM prediction models do not explain the problems of
395 LSTM hidden layers and the prediction accuracy or the relationship between them.

396

397 3.3 Hybrid ARIMA-SVR, LS-SVR and ARIMA-LSTM model prediction results

398 The flow of the ARIMA, SVR and LSTM modeling processes were described
399 sections 2.2.2, 2.2.3 and 2.2.4, respectively, and the SPEI values were predicted
400 separately. This paper proposes the ARIMA-LSTM hybrid model. Specifically, the
401 ARIMA model was used to extract the linear features of the multitime scale SPEI.
402 The residual between the predicted value and actual value of the ARIMA model were
403 entered into the LSTM model for prediction, and the advantages of the deep learning
404 method for time series were used to extract the nonlinear features. The linear part and
405 nonlinear part were combined to obtain the prediction results of the hybrid ARIMA-
406 LSTM model, and the flow chart is shown in Fig. 4. The results are shown in Fig. 9.

407 At the same time, four kinds of experimental evaluation indices were selected in this
408 paper. The hybrid ARIMA-LSTM model proposed in this paper was compared with
409 the ARIMA, SVR, LSTM, ARIMA-SVR and LS-SVR model. The feasibility of the
410 hybrid ARIMA-LSTM model for SPEI forecasting was verified. The effectiveness is
411 shown in Table 4 and Table 5.

412 Figs. 8-9 show that the predicted accuracy of the SPEI of the hybrid ARIMA-
413 LSTM model at all scales is higher than that of the single ARIMA, SVR, LSTM and
414 hybrid ARIMA-SVR, LS-SVR model. With the increase in the time scale, the
415 precision of the hybrid ARIMA-LSTM model increases gradually because the
416 precision values of the single models increase gradually. Xu et al. (2020) combined
417 the ARIMA model and SVR model and predicted multiscale SPI by using a hybrid
418 model and a single ARIMA model. This paper is similar in that the hybrid linear
419 model and nonlinear model is used for multiscale prediction, and the difference is that
420 this paper is mainly aimed at improving the short-term prediction accuracy and
421 avoiding model overfitting by using a regularization method, so it is more applicable.

422 It can be seen from Fig. 5 that the severe drought in the past 10 years in 7 sub-
423 regions of China occurred in 2014 and 2015. The EBK method was used to
424 demonstrate the spatial distribution of the model prediction results of SPEI12 in China
425 in 2014-2015, as shown in Fig. 10. It was found that the prediction accuracy of the
426 three hybrid models (ARIMA-SVR, LS-SVR and ARIMA-LSTM) is similar in spatial
427 distribution. It can be seen from Fig.9 and Table 5, the prediction accuracy of SPEI6,

428 SPEI12 and SPEI24 of the ARIMA-LSTM model is highest, indicating that the
429 ARIMA-LSTM model is suitable for long-term drought prediction.

430

431 4. Conclusions

432 In this paper, the six prediction models (ARIMA, SVR, LSTM, ARIMA-SVR,
433 LS-SVR, ARIMA-LSTM) are selected based on their advantages of predicting
434 multiscale SPEI in 7 sub-regions of China. Four evaluation indices were selected to
435 evaluate the prediction accuracy of the three models in the 1-2-month lead time, and
436 the spatial distribution of the prediction results of the three models was displayed in
437 combination with the EBK method.

438 Based on the key statistical parameters, the performance of the three hybrid
439 models (ARIMA-SVR, LS-SVR, ARIMA-LSTM) increases gradually with increasing
440 time scale. And the Prediction accuracy of the three hybrid models is higher than that
441 of the three single models (ARIMA, SVR, LSTM). According to Table 4, we can see
442 that the prediction accuracy of hybrid ARIMA-LSTM model is the highest at each
443 timescale, especially at 6-,12-, and 24 months. When the lead time was one month, the
444 prediction accuracy of hybrid ARIMA-LSTM model was lowest at SPEI1 and highest
445 at SPI24 and SPEI24. When the prediction area remains unchanged, we find that the
446 prediction accuracy of the three hybrid models decreases at all time scales with the
447 increases in the prediction advance period; that is, the prediction accuracy of the
448 model with a one-month lead time is higher than that of the model with a two-month

449 lead time. From the spatial distribution diagram of the prediction model, the hybrid
450 ARIMA-LSTM model has higher prediction accuracy than the other models,
451 indicating that the hybrid model can contribute to improving the short-term prediction
452 accuracy and more suitable of long-term scale drought in China of meteorological
453 drought.

454

455 Declarations

456 ● Ethics approval and consent to participate

457 Not applicable

458 ● Consent for publication

459 Not applicable

460 ● Availability of data and materials

461 The datasets used and/or analysed during the current study are available from the
462 corresponding author on reasonable request

463 ● Authors Contributions

464 Q.Z conceived and designed the study. Y.D and D.Z collected data. Q.Z and D.X
465 conducted the simulations and performed the analyses, also provided critical
466 insights on the results interpretation. Q.Z wrote the initial draft of the paper, with
467 substantial contributions from all authors.

468 ● Funding

469 This research was supported by State Key Laboratory of GeoInformation

470 Engineering (No.SKLGIE2019-Z-4-2). We also thank the Meteorological Data
471 Sharing Service Network in China for providing the weather data.

472 The authors declare that they have no known competing financial interests or personal
473 relationships that could have appeared to influence the work reported in this paper.

474

475

476 References:

477 Adamowski JF (2008) Development of a short-term river flood forecasting method for
478 snowmelt driven floods based on wavelet and cross-wavelet analysis. *J Hydrol*
479 353:247–266. <https://doi.org/10.1016/j.jhydrol.2008.02.013>

480 Afzali A, Keshtkar H, Pakzad S, et al (2016) Spatio-Temporal Analysis of Drought
481 Severity Using Drought Indices and Deterministic and Geostatistical Methods
482 (Case Study: Zayandehroud River Basin). *Desert* 21:165–172.
483 <https://doi.org/10.22059/jdesert.2016.60325>

484 Aiguo D, Kevin ET, Taotao Q (2004) A Global Dataset of Palmer Drought Severity
485 Index for 1870 – 2002 : Relationship with Soil Moisture and Effects of Surface
486 Warming. *J Hydrometeorol* 5:1117–1130.
487 <https://doi.org/10.1016/j.molcel.2017.04.015>

488 Belayneh A, Adamowski J (2012) Standard Precipitation Index Drought Forecasting
489 Using Neural Networks, Wavelet Neural Networks, and Support Vector
490 Regression. *Appl Comput Intell Soft Comput* 2012:1–13.
491 <https://doi.org/10.1155/2012/794061>

492 Belayneh A, Adamowski J, Khalil B, Quilty J (2016) Coupling machine learning
493 methods with wavelet transforms and the bootstrap and boosting ensemble
494 approaches for drought prediction. *Atmos Res* 172–173:37–47.
495 <https://doi.org/10.1016/j.atmosres.2015.12.017>

496 Bhuiyan C, Singh RP, Kogan FN (2006) Monitoring drought dynamics in the Aravalli
497 region (India) using different indices based on ground and remote sensing data.
498 *Int J Appl Earth Obs Geoinf* 8:289–302.
499 <https://doi.org/10.1016/j.jag.2006.03.002>

500 Borji M, Malekian A, Salajegheh A, Ghadimi M (2016) Multi-time-scale analysis of
501 hydrological drought forecasting using support vector regression (SVR) and
502 artificial neural networks (ANN). *Arab J Geosci* 9:
503 <https://doi.org/10.1007/s12517-016-2750-x>

504 Cai X, Wang X, Jain P, Flannigan MD (2019) Evaluation of Gridded Precipitation
505 Data and Interpolation Methods for Forest Fire Danger Rating in Alberta,
506 Canada. *J Geophys Res Atmos* 124:3–17. <https://doi.org/10.1029/2018JD028754>

507 Chen H, Sun J (2015) Changes in drought characteristics over china using the
508 standardized precipitation evapotranspiration index. *J Clim* 28:5430–5447.
509 <https://doi.org/10.1175/JCLI-D-14-00707.1>

510 Chen S, Shin JY, Kim TW (2017) Probabilistic forecasting of drought: a hidden
511 Markov model aggregated with the RCP 8.5 precipitation projection. *Stoch*

512 Environ Res Risk Assess 31:1061–1076. <https://doi.org/10.1007/s00477-016->
513 1279-6

514 Choubin B, Malekian A (2017) Combined gamma and M-test-based ANN and
515 ARIMA models for groundwater fluctuation forecasting in semiarid regions.
516 Environ Earth Sci 76:. <https://doi.org/10.1007/s12665-017-6870-8>

517 Choubin B, Malekian A, Golshan M (2016) Application of several data-driven
518 techniques to predict a standardized precipitation index. Atmosfera 29:121–128.
519 <https://doi.org/10.20937/ATM.2016.29.02.02>

520 Deo RC, Şahin M (2015) Application of the Artificial Neural Network model for
521 prediction of monthly Standardized Precipitation and Evapotranspiration Index
522 using hydrometeorological parameters and climate indices in eastern Australia.
523 Atmos Res 161–162:65–81. <https://doi.org/10.1016/j.atmosres.2015.03.018>

524 Deo RC, Şahin M (2016) An extreme learning machine model for the simulation of
525 monthly mean streamflow water level in eastern Queensland. Environ Monit
526 Assess 188:1–24. <https://doi.org/10.1007/s10661-016-5094-9>

527 Fung KF, Huang YF, Koo CH (2019a) Coupling fuzzy–SVR and boosting–SVR
528 models with wavelet decomposition for meteorological drought prediction.
529 Environ Earth Sci 78:1–18. <https://doi.org/10.1007/s12665-019-8700-7>

530 Fung KF, Huang YF, Koo CH, Soh YW (2019b) Drought forecasting: A review of
531 modelling approaches 2007–2017. J Water Clim Chang.
532 <https://doi.org/10.2166/wcc.2019.236>

533 Gao Y, Markkanen T, Thum T, et al (2016) Assessing various drought indicators in
534 representing summer drought in boreal forests in Finland. *Hydrol Earth Syst Sci*
535 20:175–191. <https://doi.org/10.5194/hess-20-175-2016>

536 Gu Y, Brown JF, Verdin JP, Wardlow B (2007) A five-year analysis of MODIS
537 NDVI and NDWI for grassland drought assessment over the central Great Plains
538 of the United States. *Geophys Res Lett* 34:1–6.
539 <https://doi.org/10.1029/2006GL029127>

540 Han P, Wang PX, Zhang SY, Zhu DH (2010) Drought forecasting based on the
541 remote sensing data using ARIMA models. *Math Comput Model* 51:1398–1403.
542 <https://doi.org/10.1016/j.mcm.2009.10.031>

543 Hayes MJ, Wilhite DA, Vanyarkho O V (1996) Monitoring the 1996 Drought Using
544 the Standardized Precipitation Index. *Bull Am Meteorol Soc* 429–438

545 Hochreiter S (1997) Long Short-Term Memory. 1780:1735–1780

546 Hu W, Tong S, Mengersen K, Connell D (2007) Weather Variability and the
547 Incidence of Cryptosporidiosis: Comparison of Time Series Poisson Regression
548 and SARIMA Models. *Ann Epidemiol* 17:679–688.
549 <https://doi.org/10.1016/j.annepidem.2007.03.020>

550 Jain P, Flannigan MD (2017) Comparison of methods for spatial interpolation of fire
551 weather in Alberta, Canada. *Can J For Res* 47:1646–1658.
552 <https://doi.org/10.1139/cjfr-2017-0101>

553 Jeong J, Park E (2019) Comparative applications of data-driven models representing
554 water table fluctuations. *J Hydrol* 572:261–273.
555 <https://doi.org/10.1016/j.jhydrol.2019.02.051>

556 Karavitis CA, Chortaria C, Alexandris S, et al (2012) Development of the
557 standardised precipitation index for Greece. *Urban Water J* 9:401–417.
558 <https://doi.org/10.1080/1573062X.2012.690431>

559 Karthika M, Krishnaveni, Thirunavukkarasu V (2017) Forecasting of meteorological
560 drought using ARIMA model. *Indian J Agric Res* 51:103–111.
561 <https://doi.org/10.18805/ijare.v0i0F.7631>

562 Kisi O, Sanikhani H, Zounemat-Kermani M, Niazi F (2015) Long-term monthly
563 evapotranspiration modeling by several data-driven methods without climatic
564 data. *Comput Electron Agric* 115:66–77.
565 <https://doi.org/10.1016/j.compag.2015.04.015>

566 Kousari MR, Hosseini ME, Ahani H, Hakimelahi H (2017) Introducing an operational
567 method to forecast long-term regional drought based on the application of
568 artificial intelligence capabilities. *Theor Appl Climatol* 127:361–380.
569 <https://doi.org/10.1007/s00704-015-1624-6>

570 Li L, She D, Zheng H, et al (2020) Elucidating Diverse Drought Characteristics from
571 Two Meteorological Drought Indices (SPI and SPEI) in China. *J Hydrometeorol*
572 21:1513–1530. <https://doi.org/10.1175/jhm-d-19-0290.1>

573 Manatsa D, Chingombe W, Matarira CH (2008) The impact of the positive Indian
574 Ocean dipole on Zimbabwe droughts Tropical climate is understood to be
575 dominated by. *Int J Climatol* 2029:2011–2029. <https://doi.org/10.1002/joc>
576 Marj AF, Meijerink AMJ (2011) Agricultural drought forecasting using satellite
577 images, climate indices and artificial neural network. *Int J Remote Sens*
578 32:9707–9719. <https://doi.org/10.1080/01431161.2011.575896>
579 Mckee TB, Doesken NJ, Kleist J (1993) The relationship of drought frequency and
580 duration to time scales. Eighth Conf. Appl. Climatol. 17-22 January 1993,
581 Anaheim, Calif. 179:17–22
582 Mishra AK, Desai VR (2005) Drought forecasting using stochastic models. *Stoch*
583 *Environ Res Risk Assess* 19:326–339. [https://doi.org/10.1007/s00477-005-0238-](https://doi.org/10.1007/s00477-005-0238-4)
584 4
585 Mishra AK, Desai VR (2006) Drought forecasting using feed-forward recursive
586 neural network. *Ecol Modell* 198:127–138.
587 <https://doi.org/10.1016/j.ecolmodel.2006.04.017>
588 Mishra AK, Desai VR, Singh VP (2007) Drought Forecasting Using a Hybrid
589 Stochastic and Neural Network Model. *J Hydrol Eng* 12:626–638.
590 [https://doi.org/10.1061/\(ASCE\)1084-0699\(2007\)12:6\(626\)](https://doi.org/10.1061/(ASCE)1084-0699(2007)12:6(626))
591 Modaresi F, Araghinejad S, Ebrahimi K (2018) A Comparative Assessment of
592 Artificial Neural Network, Generalized Regression Neural Network, Least-
593 Square Support Vector Regression, and K-Nearest Neighbor Regression for

594 Monthly Streamflow Forecasting in Linear and Nonlinear Conditions. *Water*
595 *Resour Manag* 32:243–258. <https://doi.org/10.1007/s11269-017-1807-2>

596 Mossad A, Alazba AA (2015) Drought forecasting using stochastic models in a hyper-
597 arid climate. *Atmosphere (Basel)* 6:410–430.
598 <https://doi.org/10.3390/atmos6040410>

599 Narasimhan B, Srinivasan R (2005) Development and evaluation of Soil Moisture
600 Deficit Index (SMDI) and Evapotranspiration Deficit Index (ETDI) for
601 agricultural drought monitoring. *Agric For Meteorol* 133:69–88.
602 <https://doi.org/10.1016/j.agrformet.2005.07.012>

603 Ochoa-Rivera JC (2008) Prospecting droughts with stochastic artificial neural
604 networks. *J Hydrol* 352:174–180. <https://doi.org/10.1016/j.jhydrol.2008.01.006>

605 Paulo AA, Rosa RD, Pereira LS (2012) Climate trends and behaviour of drought
606 indices based on precipitation and evapotranspiration in Portugal. *Nat Hazards*
607 *Earth Syst Sci* 12:1481–1491. <https://doi.org/10.5194/nhess-12-1481-2012>

608 Poornima S, Pushpalatha M (2019) Drought prediction based on SPI and SPEI with
609 varying timescales using LSTM recurrent neural network. *Soft Comput* 1:.
610 <https://doi.org/10.1007/s00500-019-04120-1>

611 Qi Y, Li Q, Karimian H, Liu D (2019) A hybrid model for spatiotemporal forecasting
612 of PM 2.5 based on graph convolutional neural network and long short-term
613 memory. *Sci Total Environ* 664:1–10.
614 <https://doi.org/10.1016/j.scitotenv.2019.01.333>

615 Rafiei-Sardooi E, Mohseni-Saravi M, Barkhori S, et al (2018) Drought modeling: a
616 comparative study between time series and neuro-fuzzy approaches. Arab J
617 Geosci 11:. <https://doi.org/10.1007/s12517-018-3835-5>

618 Salman AG, Heryadi Y, Abdurahman E, Suparta W (2018) Weather forecasting using
619 merged Long Short-Term Memory Model (LSTM) and Autoregressive
620 Integrated Moving Average (ARIMA) Model. J Comput Sci 14:930–938.
621 <https://doi.org/10.3844/jcssp.2018.930.938>

622 Seibert M, Merz B, Apel H (2017) Seasonal forecasting of hydrological drought in the
623 Limpopo Basin: A comparison of statistical methods. Hydrol Earth Syst Sci
624 21:1611–1629. <https://doi.org/10.5194/hess-21-1611-2017>

625 Sigaroodi SK, Chen Q, Ebrahimi S, et al (2013) Long-term precipitation forecast for
626 drought relief using atmospheric circulation factors: a study on the Maharloo
627 Basin in Iran. Hydrol Earth Syst Sci Discuss 10:13333–13361.
628 <https://doi.org/10.5194/hessd-10-13333-2013>

629 Soh YW, Koo CH, Huang YF, Fung KF (2018) Application of artificial intelligence
630 models for the prediction of standardized precipitation evapotranspiration index
631 (SPEI) at Langat River Basin, Malaysia. Comput Electron Agric 144:164–173.
632 <https://doi.org/10.1016/j.compag.2017.12.002>

633 Suykens JAK, De Brabanter J, Lukas L, Vandewalle J (2002) Weighted least squares
634 support vector machines: Robustness and sparse approximation.
635 Neurocomputing 48:85–105. [https://doi.org/10.1016/S0925-2312\(01\)00644-0](https://doi.org/10.1016/S0925-2312(01)00644-0)

- 636 Tatli H, Türkeş M (2011) Empirical Orthogonal Function analysis of the palmer
637 drought indices. *Agric For Meteorol* 151:981–991.
638 <https://doi.org/10.1016/j.agrformet.2011.03.004>
- 639 Tian M, Wang P, Khan J (2016) Drought forecasting with vegetation temperature
640 condition index using arima models in the guanzhong plain. *Remote Sens* 8:.
641 <https://doi.org/10.3390/rs8090690>
- 642 Tian Y, Xu YP, Wang G (2018) Agricultural drought prediction using climate indices
643 based on Support Vector Regression in Xiangjiang River basin. *Sci Total*
644 *Environ* 622–623:710–720. <https://doi.org/10.1016/j.scitotenv.2017.12.025>
- 645 Tran Anh D, Van SP, Dang TD, Hoang LP (2019) Downscaling rainfall using deep
646 learning long short-term memory and feedforward neural network. *Int J*
647 *Climatol*. <https://doi.org/10.1002/joc.6066>
- 648 Vicente-Serrano SM, Beguería S, López-Moreno JI (2010) A multiscalar drought
649 index sensitive to global warming: The standardized precipitation
650 evapotranspiration index. *J Clim* 23:1696–1718.
651 <https://doi.org/10.1175/2009JCLI2909.1>
- 652 Vicente-Serrano SM, Van der Schrier G, Beguería S, et al (2015) Contribution of
653 precipitation and reference evapotranspiration to drought indices under different
654 climates. *J Hydrol* 526:42–54. <https://doi.org/10.1016/j.jhydrol.2014.11.025>
- 655 Wang H, Vicente-serrano SM, Tao F, et al (2016) Monitoring winter wheat drought
656 threat in Northern China using multiple climate-based drought indices and soil

657 moisture during 2000–2013. *Agric For Meteorol* 228–229:1–12.
658 <https://doi.org/10.1016/j.agrformet.2016.06.004>

659 Wang Q, Shi P, Lei T, et al (2015) The alleviating trend of drought in the Huang-
660 Huai-Hai Plain of China based on the daily SPEI. *Int J Climatol* 35:3760–3769.
661 <https://doi.org/10.1002/joc.4244>

662 Xu D, Zhang Q, Ding Y, Huang H (2020a) Application of a hybrid ARIMA-SVR
663 model based on the SPI for the forecast of drought—A case study in Henan
664 Province, China. *J Appl Meteorol Climatol*. [https://doi.org/10.1175/jamc-d-19-](https://doi.org/10.1175/jamc-d-19-0270.1)
665 [0270.1](https://doi.org/10.1175/jamc-d-19-0270.1)

666 Xu D, Zhang Q, Ding Y, Huang H (2020b) Application of a Hybrid ARIMA–SVR
667 Model Based on the SPI for the Forecast of Drought—A Case Study in Henan
668 Province, China. *J Appl Meteorol Climatol* 59:1239–1259.
669 <https://doi.org/10.1175/jamc-d-19-0270.1>

670 Yao J, Zhao Y, Chen Y, et al (2018a) Multi-scale assessments of droughts: A case
671 study in Xinjiang, China. *Sci Total Environ* 630:444–452.
672 <https://doi.org/10.1016/j.scitotenv.2018.02.200>

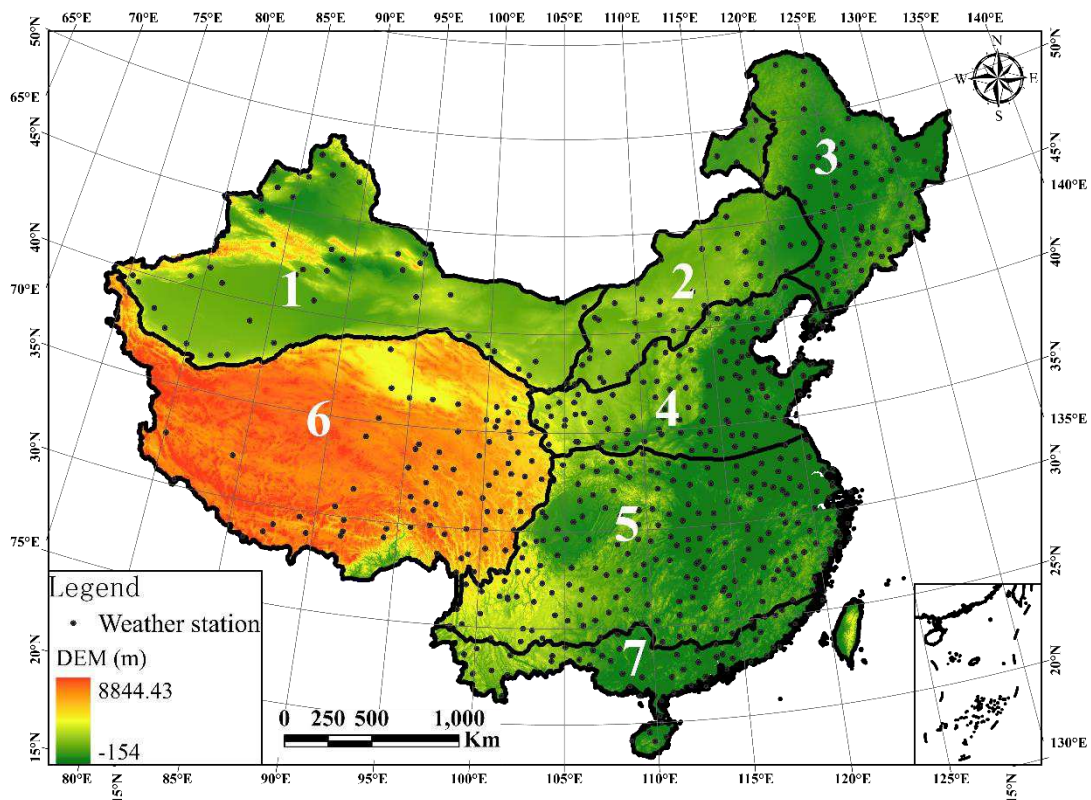
673 Yao N, Li Y, Lei T, Peng L (2018b) Drought evolution, severity and trends in
674 mainland China over 1961–2013. *Sci Total Environ* 616–617:73–89.
675 <https://doi.org/10.1016/j.scitotenv.2017.10.327>

676 Yurekli K, Kurunc A, Ozturk F (2005) Application of linear stochastic models to
677 monthly flow data of Kelkit Stream. *Ecol Modell* 183:67–75.
678 <https://doi.org/10.1016/j.ecolmodel.2004.08.001>

679 Zhang J, Zhu Y, Zhang X, et al (2018) Developing a Long Short-Term Memory
680 (LSTM) based model for predicting water table depth in agricultural areas. *J*
681 *Hydrol* 561:918–929. <https://doi.org/10.1016/j.jhydrol.2018.04.065>

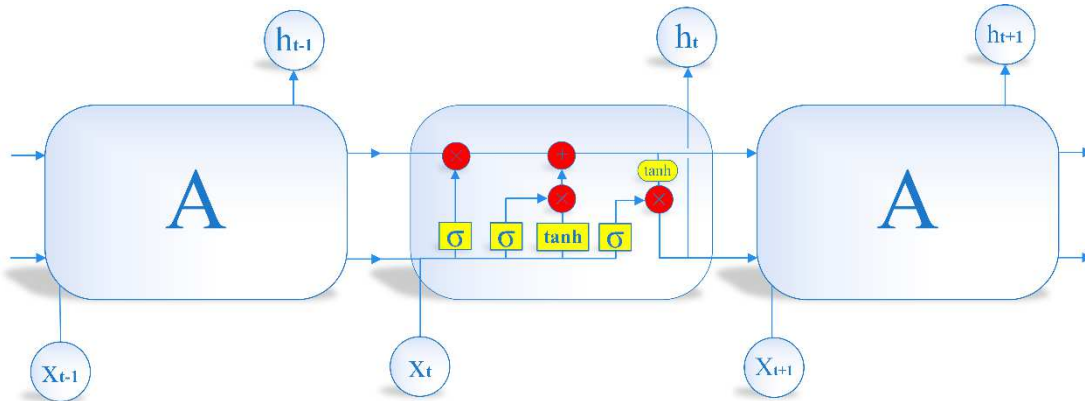
682 Zhang R, Chen ZY, Xu LJ, Ou CQ (2019) Meteorological drought forecasting based
683 on a statistical model with machine learning techniques in Shaanxi province,
684 China. *Sci Total Environ* 665:338–346.
685 <https://doi.org/10.1016/j.scitotenv.2019.01.431>

686



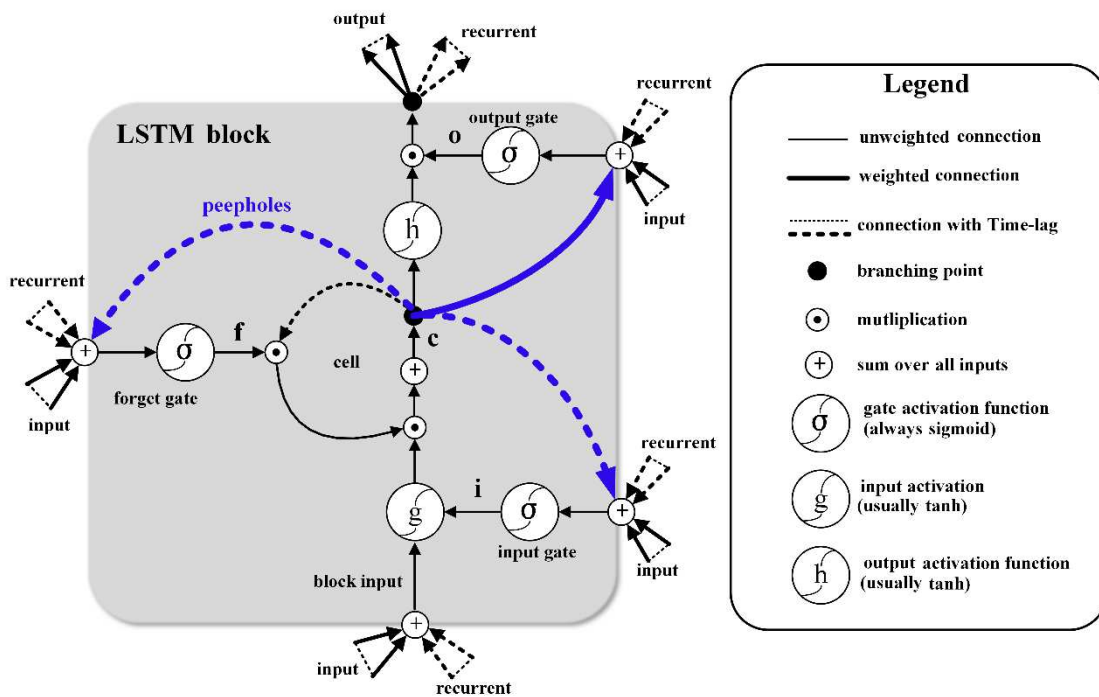
687

688 Fig.1. Geological information, DEM, station distribution and sub-region division in
 689 China. The numbers in the map denotes different sub-regions.



690

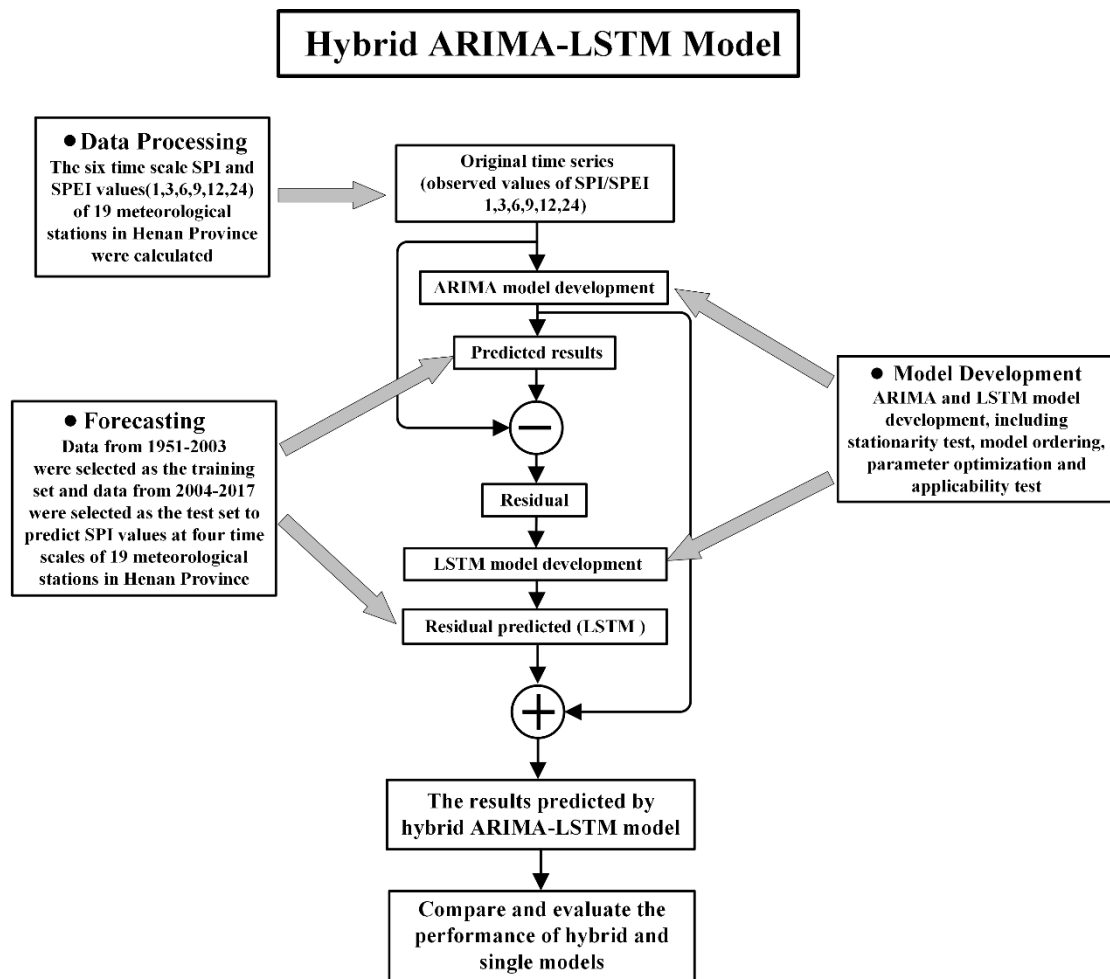
691 Fig.2. Four interaction layers of the LSTM module chain.



692

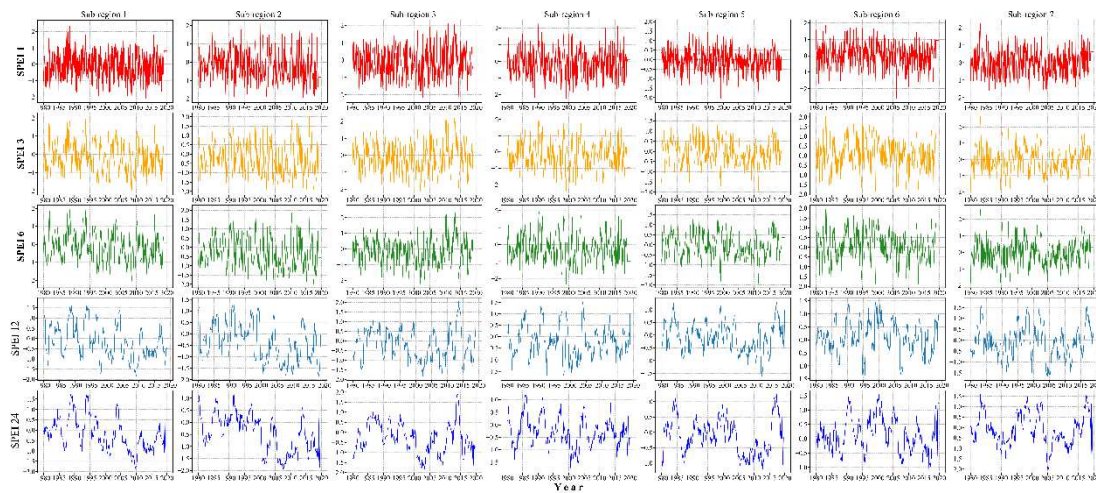
693

694 Fig.3. LSTM cell structure in hidden layer.



695

696 Fig.4. hybrid ARIMA-LSTM model flow chart.



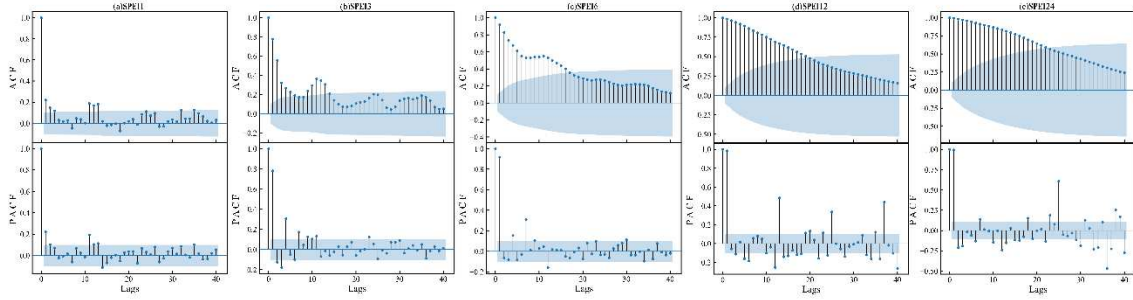
697

698 Fig.5. The variations of SPEI at the 1-, 3-, 6-, 12- and 24-month timescales over

699 1980–2013 in 7 sub-regions of China.

700

701

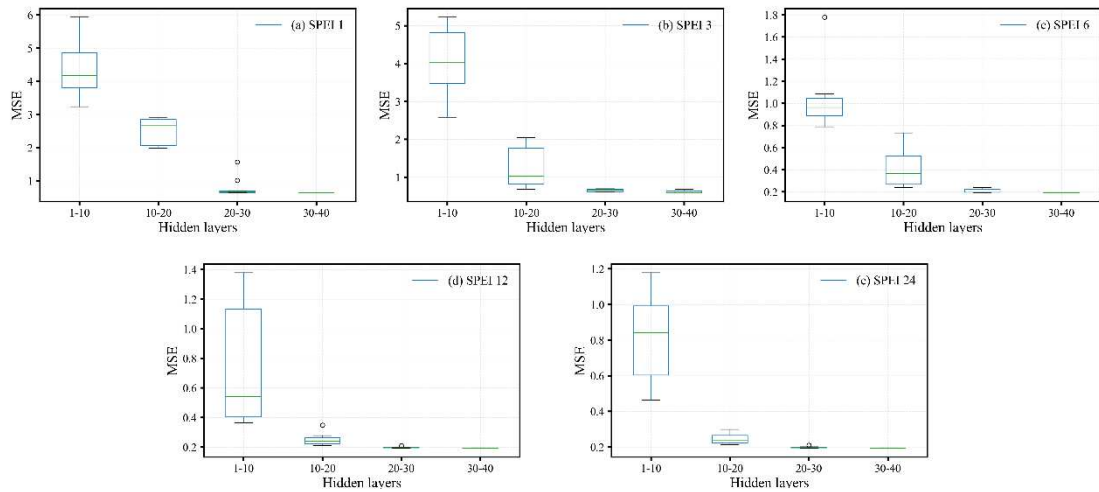


702

703 Fig.6. ACF and PACF of SPEI at the 1-, 3-, 6-, 12- and 24-month timescales in sub-

704 region 1 of China.

705



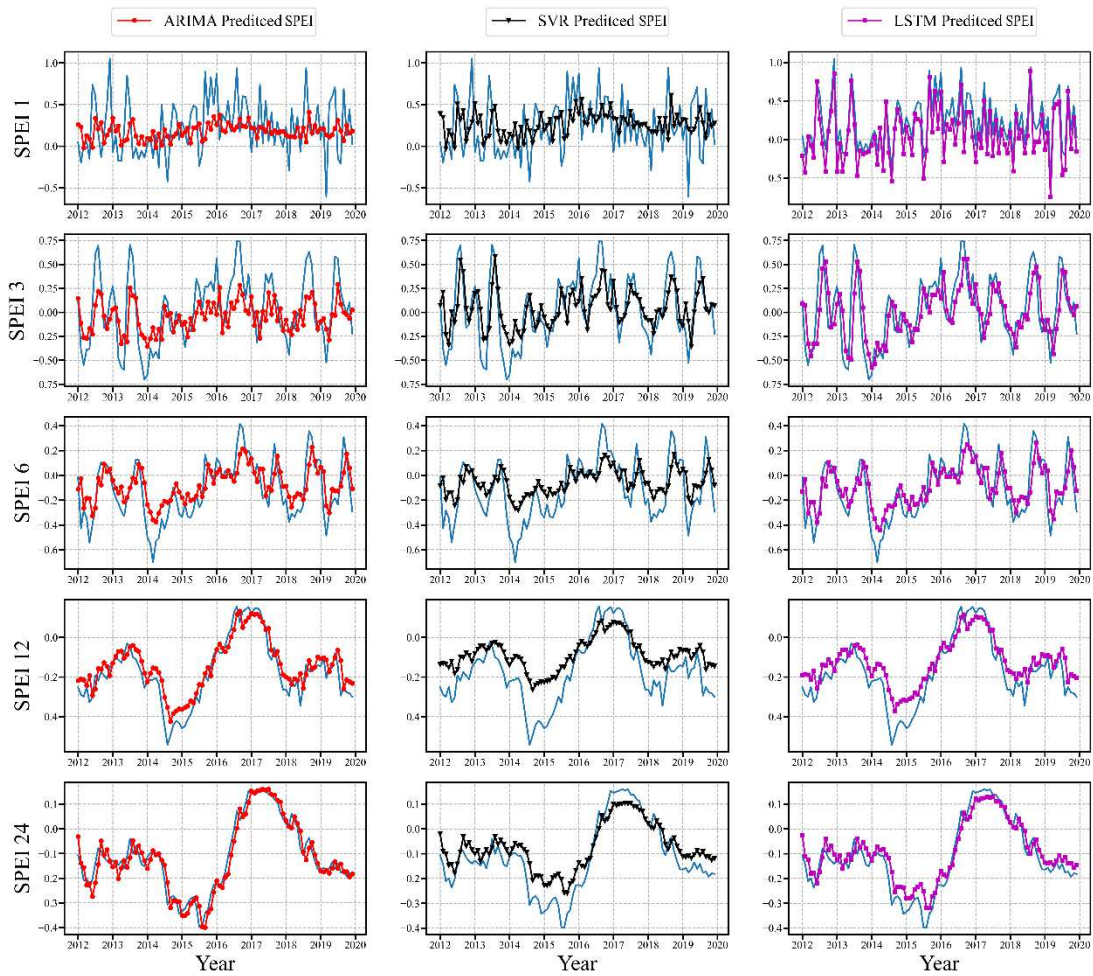
706

707 Fig.7 Multitime scale boxplot of loss fuction and hidden layers of SPEI in sub-region

708 1 of China.

709

710



711

712 Fig.8. Forecast of multitime scale SPEI value of ARIMA model, SVR model and

713 LSTM model.

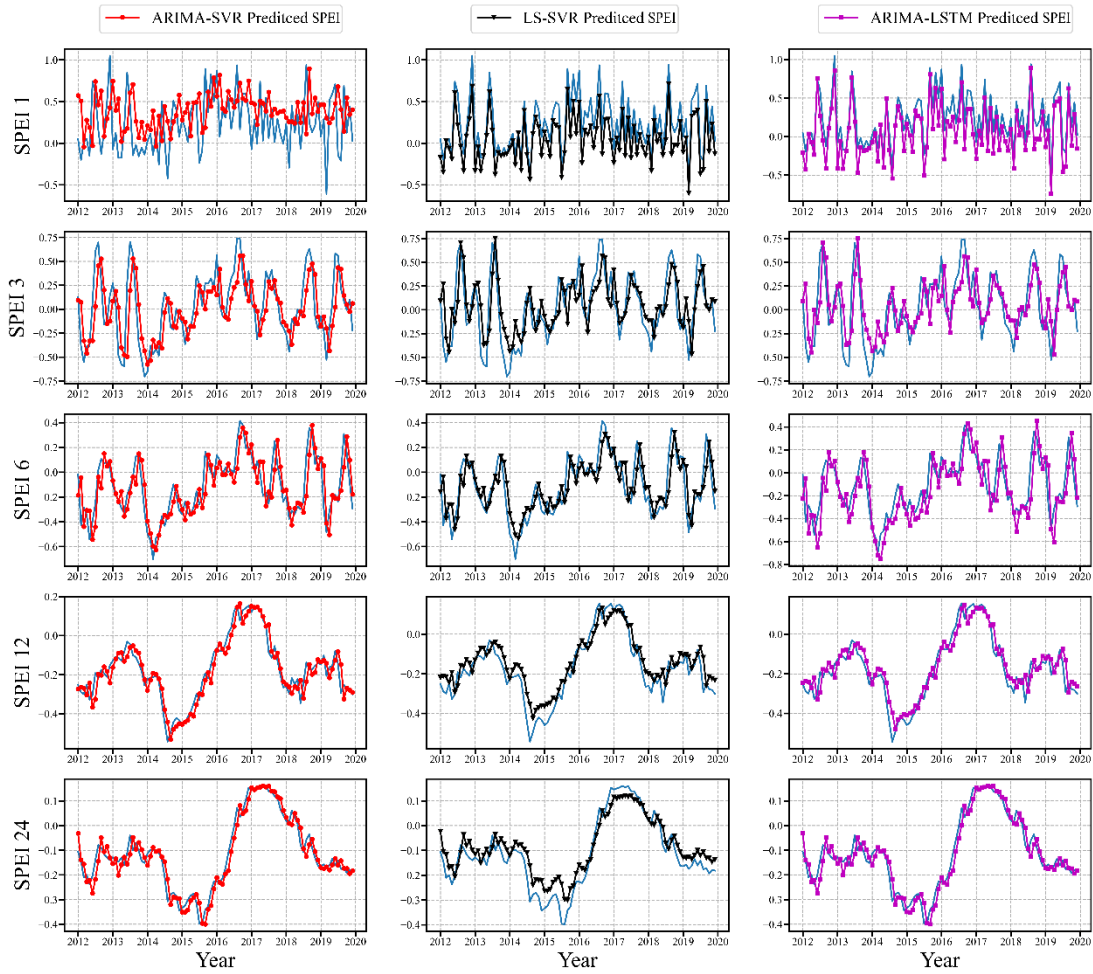
714

715

716

717

718

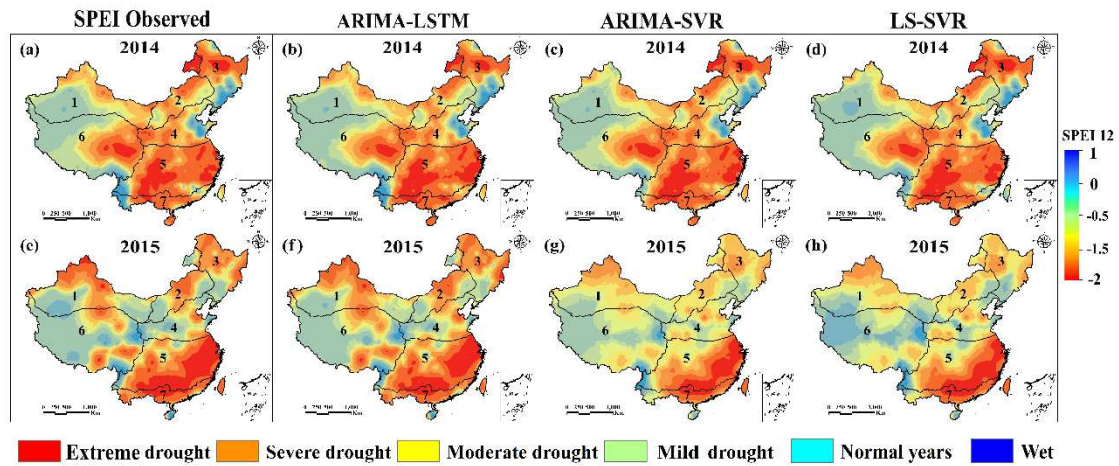


719

720 Fig.9. Forecast of multitime scale SPEI value of hybrid ARIMA-SVR model, LS-

721 SVR model and ARIMA-LSTM model.

722



723

724 Fig.10. Spatial distributions of SPEI drought levels in 2014 and 2015, using the three

725 forecasting models (ARIMA-SVR, LS-SVR and ARIMA-LSTM model).

726

727 Table 1

728 Drought level classification using SPEI.

Level	Type	Range of SPEI
0	Wet	$0.5 \leq \text{SPEI}$
1	No drought	$-0.5 \leq \text{SPEI} < 0.5$
2	Mild drought	$-1.0 \leq \text{SPEI} < -0.5$
3	Moderate drought	$-1.5 \leq \text{SPEI} < -1.0$
4	Severe drought	$-2.0 \leq \text{SPEI} < -1.5$
5	Extreme drought	$\text{SPEI} \leq -2.0$

729

730 Table 2

731 Unit root test of 7 sub-regions at five time scales of the SPEI original sequence.

SPEI series	Sub-region1		Sub-region2		Sub-region3		Sub-region4		Sub-region5		Sub-region6		Sub-region7	
	ADF	P-value												
SPEI-1	-3.834	2.57E-03	-17.395	4.97E-30	-12.979	2.97E-24	-17.759	3.34E-30	-18.672	2.04E-30	-18.006	2.72E-30	-17.46	4.58E-30
SPEI-3	-2.803	5.78E-02	-9.068	4.36E-15	-7.654	1.75E-11	-8.092	1.36E-12	-7.513	3.94E-11	-4.337	3.81E-04	-6.842	1.78E-09
SPEI-6	-2.587	9.55E-02	-4.777	6.01E-05	-6.398	2.02E-08	-4.217	6.10E-04	-4.545	1.62E-04	-5.281	5.97E-06	-3.765	3.27E-03
SPEI-12	-2.671	7.90E-02	-2.342	1.59E-01	-3.5	7.98E-03	-2.656	8.18E-02	-3.664	4.64E-03	-6.953	9.56E-10	-3.584	6.07E-03
SPEI-24	-2.335	1.61E-01	-2.026	2.75E-01	-3.738	3.60E-03	-2.53	0.10829	-4.694	8.62E-05	-4.462	2.29E-04	-3.014	3.36E-02

732

733
734
735
736

Table 3
AIC, BIC, HQIC and $P_{Ljung-Box}$ test comparisons of selected models at five-time scale of SPEI for 7 sub-regions.

SPEI series	Example Stations	Model	AIC	BIC	HQIC	$P_{Ljung-Box}$
SPEI-1	Sub-region1	ARIMA(3,0,5)(1,0,2) ₁	2248.092	234.352	2269.701	0.996
	Sub-region2	ARIMA(3,0,3)(0,0,1) ₁	719.718	753.092	732.838	0.886
	Sub-region3	ARIMA(3,0,5)(1,0,0) ₁	905.207	917.722	910.127	0.981
	Sub-region4	ARIMA(3,0,3)(1,0,0) ₁	732.199	744.714	737.119	0.985
	Sub-region5	ARIMA(4,0,2)(0,0,1) ₁	594.122	627.495	607.241	0.945
	Sub-region6	ARIMA(3,0,5)(1,0,0) ₁	293.753	306.286	298.673	0.914
	Sub-region7	ARIMA(1,0,0) ₁	829.772	842.287	834.692	0.959
SPEI-3	Sub-region1	ARIMA(2,0,3)(1,0,3) ₃	156.527	181.556	166.367	0.457
	Sub-region2	ARIMA(5,0,4)(0,0,2) ₃	335.71	381.599	353.749	0.994
	Sub-region3	ARIMA(2,0,4)(0,0,2) ₃	565.241	581.928	571.801	0.716
	Sub-region4	ARIMA(1,0,2) ₃	335.785	356.644	343.985	0.81
	Sub-region5	ARIMA(5,0,4)(2,0,0) ₃	255.756	272.443	262.316	0.315
	Sub-region6	ARIMA(2,0,5)(1,0,3) ₃	94.575	119.605	104.415	0.227
	Sub-region7	ARIMA(0,0,2)(0,0,3) ₃	389.353	410.211	397.552	0.939
SPEI-6	Sub-region1	ARIMA(8,0,2)(8,0,1) ₆	116.904	66.844	97.225	0.77
	Sub-region2	ARIMA(9,0,5)(1,0,5) ₆	11.284	22.126	1.872	0.947
	Sub-region3	ARIMA(0,0,5) ₆	232.062	261.264	243.542	0.891
	Sub-region4	ARIMA(2,0,5)(1,0,5) ₆	52.585	19.212	39.466	0.785
	Sub-region5	ARIMA(0,0,5) ₆	113.02	83.818	101.541	0.824
	Sub-region6	ARIMA(9,0,5)(7,0,0) ₆	175.86	138.314	161.1	0.693
	Sub-region7	ARIMA(0,0,5) ₆	63.574	92.776	75.054	0.541
SPEI-12	Sub-region1	ARIMA(10,0,5)(9,0,5) ₁₂	473.387	419.155	452.067	0.899
	Sub-region2	ARIMA(10,0,5) ₁₂	574.376	520.144	553.057	0.975
	Sub-region3	ARIMA(10,0,5) ₁₂	335.364	281.132	314.044	0.935
	Sub-region4	ARIMA(10,0,5)(7,0,5) ₁₂	532.11	477.878	510.791	0.969
	Sub-region5	ARIMA(8,0,4)(4,0,2) ₁₂	499.37	449.309	479.69	0.666
	Sub-region6	ARIMA(10,0,5)(1,0,0) ₁₂	399.511	349.45	379.831	0.85
	Sub-region7	ARIMA(10,0,5) ₁₂	259.529	209.468	239.849	0.856
SPEI-24	Sub-region1	ARIMA(8,0,5)(2,0,1) ₂₄	625.846	604.987	617.646	0.927
	Sub-region2	ARIMA(10,0,4)(1,0,0) ₂₄	954.879	555.132	928.64	0.967
	Sub-region3	ARIMA(7,0,4)(1,0,0) ₂₄	655.885	601.653	634.566	0.952
	Sub-region4	ARIMA(6,0,4)(1,0,0) ₂₄	775.902	763.386	770.982	0.485
	Sub-region5	ARIMA(10,0,4)(3,0,2) ₂₄	701.918	672.716	690.438	0.72
	Sub-region6	ARIMA(8,0,5)(1,0,0) ₂₄	162.256	149.741	157.336	0.899
	Sub-region7	ARIMA(10,0,4)(2,0,0) ₂₄	578.841	562.155	572.282	0.941

737
738
739
740
741

Table 4
Performance measures for comparison of observed and predicted data for 1-2 month lead times for five-time scale of SPEI.

Lead times	Model	Performance measures	SPEI1	SPEI3	SPEI6	SPEI-12	SPEI-24
1-month	ARIMA	MSE	0.431	0.535	0.277	0.246	0.187
		NSE	-0.055	0.146	0.389	0.611	0.683
		RMSE	0.637	0.642	0.454	0.373	0.351
		MAE	0.634	0.596	0.507	0.318	0.304
	SVR	MSE	0.314	0.409	0.667	0.636	0.577
		NSE	0.127	0.247	0.149	0.371	0.443
		RMSE	0.548	0.468	0.824	0.743	0.721
		MAE	0.278	0.308	0.787	0.598	0.584
	LSTM	MSE	0.372	0.472	0.472	0.441	0.382
		NSE	0.036	0.196	0.269	0.491	0.563
		RMSE	0.592	0.555	0.639	0.558	0.536
		MAE	0.456	0.452	0.647	0.458	0.444
2-month	ARIMA	MSE	1.436	1.54	1.282	1.251	1.192
		NSE	-0.425	-0.224	0.019	0.241	0.313
		RMSE	1.027	1.032	0.844	0.763	0.741
		MAE	1.024	0.986	0.897	0.708	0.694
	SVR	MSE	0.704	0.799	1.057	1.026	0.967
		NSE	-0.444	-0.283	-0.211	0.011	0.083
		RMSE	1.052	1.015	1.099	1.018	0.996
		MAE	0.916	0.912	1.107	0.918	0.904
	LSTM	MSE	1.896	1.802	1.742	1.711	1.652
		NSE	-0.414	-0.253	-0.181	0.041	0.113
		RMSE	0.902	0.865	0.949	0.868	0.846
		MAE	0.866	0.862	1.057	0.868	0.854

742
743
744
745
746
747
748
749
750

751 Table 5
 752 Performance measures for comparison of observed and predicted data for 1-2 month lead
 753 times for five-time scale of SPEI.
 754
 755

Lead times	Model	Performance measures	SPEI1	SPEI3	SPEI6	SPEI-12	SPEI-24
1-month	ARIMA-SVR	MSE	0.282	0.386	0.128	0.097	0.038
		NSE	0.043	0.244	0.487	0.709	0.781
		RMSE	0.53	0.535	0.347	0.266	0.244
		MAE	0.424	0.386	0.297	0.108	0.094
	LS-SVR	MSE	0.264	0.276	0.249	0.148	0.107
		NSE	0.168	0.379	0.378	0.649	0.543
		RMSE	0.437	0.508	0.448	0.398	0.313
		MAE	0.308	0.324	0.387	0.287	0.187
	ARIMA-LSTM	MSE	0.175	0.204	0.019	0.003	0.001
		NSE	0.368	0.451	0.659	0.885	0.93
		RMSE	0.347	0.479	0.137	0.053	0.037
		MAE	0.207	0.189	0.108	0.042	0.028
2-month	ARIMA-SVR	MSE	0.772	0.876	0.618	0.587	0.528
		NSE	-0.337	-0.136	0.107	0.329	0.401
		RMSE	1.05	1.055	0.867	0.786	0.764
		MAE	0.944	0.906	0.817	0.628	0.614
	LS-SVR	MSE	0.784	0.796	0.769	0.668	0.627
		NSE	-0.372	-0.161	-0.162	0.109	0.003
		RMSE	0.907	0.978	0.918	0.868	0.783
		MAE	0.778	0.794	0.857	0.757	0.657
	ARIMA-LSTM	MSE	0.645	0.674	0.489	0.473	0.471
		NSE	0.068	0.151	0.359	0.585	0.63
		RMSE	0.817	0.949	0.607	0.523	0.507
		MAE	0.677	0.659	0.578	0.512	0.498

756

Figures

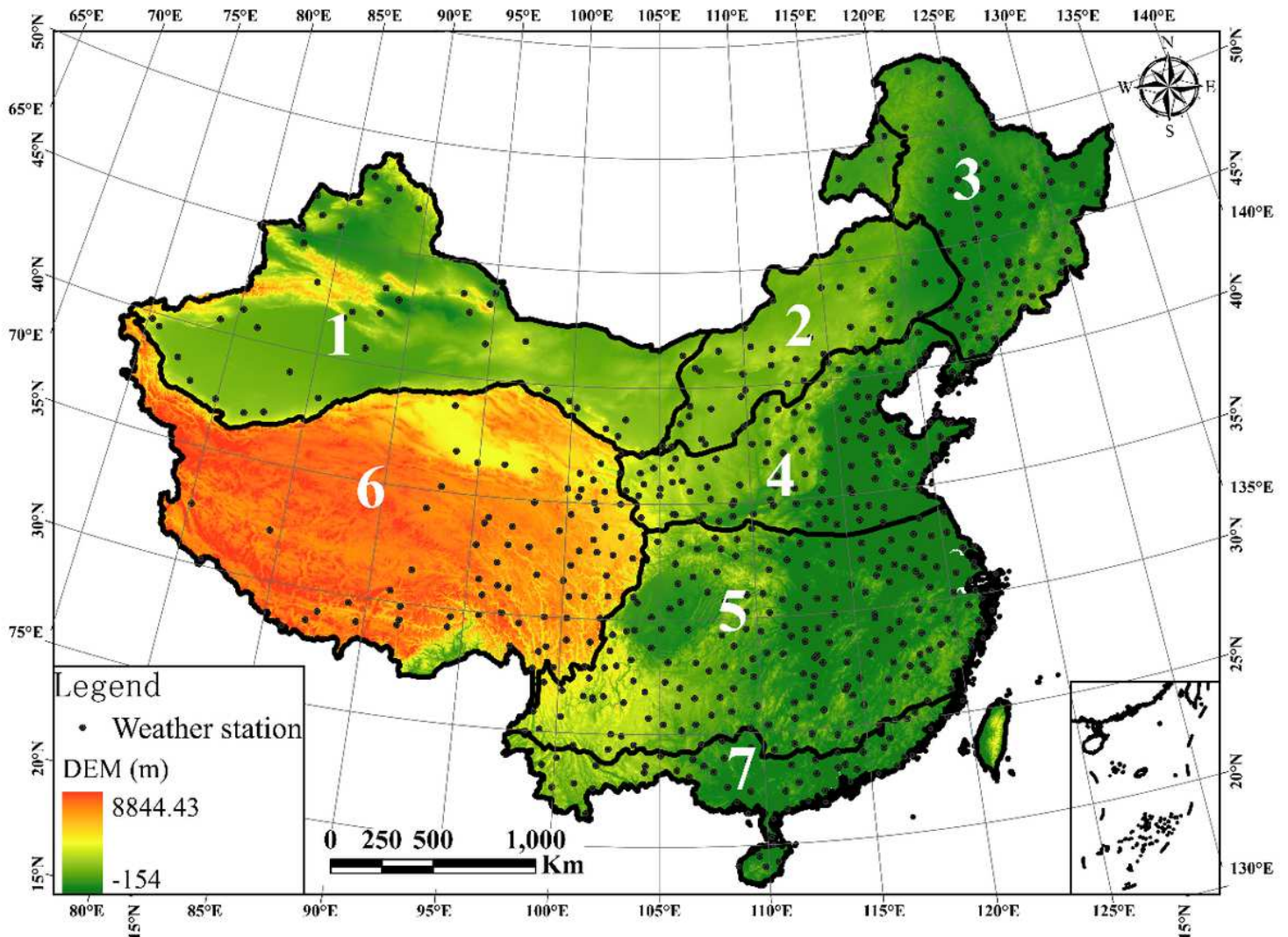


Figure 1

Geological information, DEM, station distribution and sub-region division in China. The numbers in the map denotes different sub-regions. Note: The designations employed and the presentation of the material on this map do not imply the expression of any opinion whatsoever on the part of Research Square concerning the legal status of any country, territory, city or area or of its authorities, or concerning the delimitation of its frontiers or boundaries. This map has been provided by the authors.

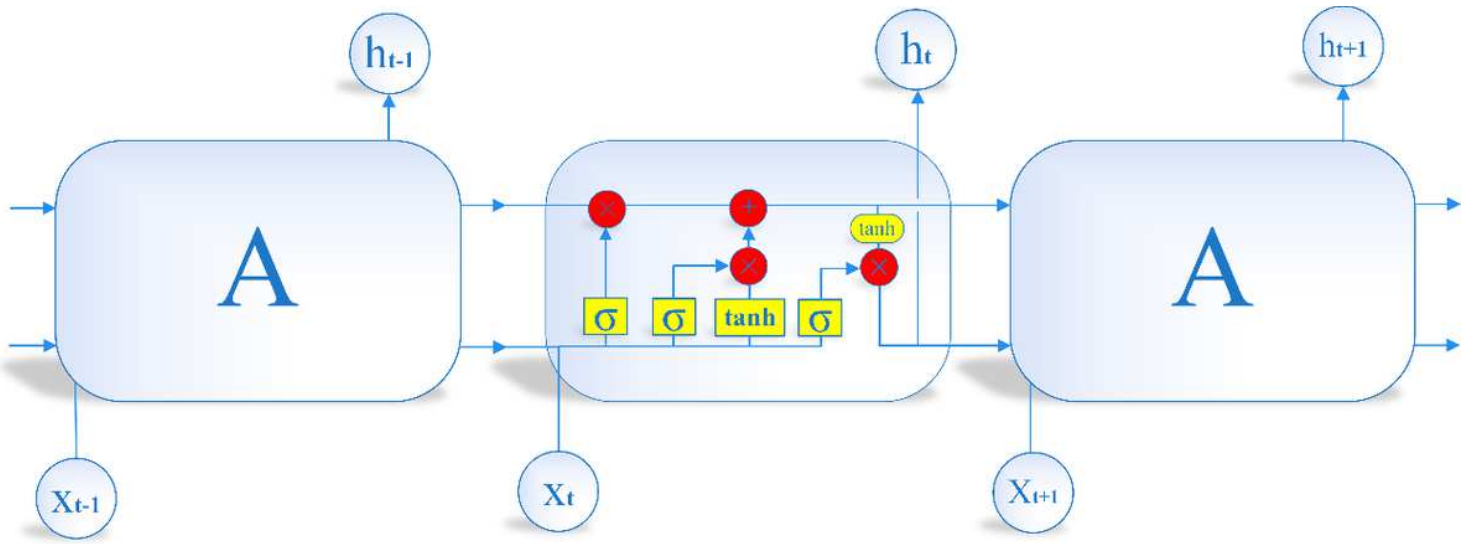


Figure 2

Four interaction layers of the LSTM module chain.

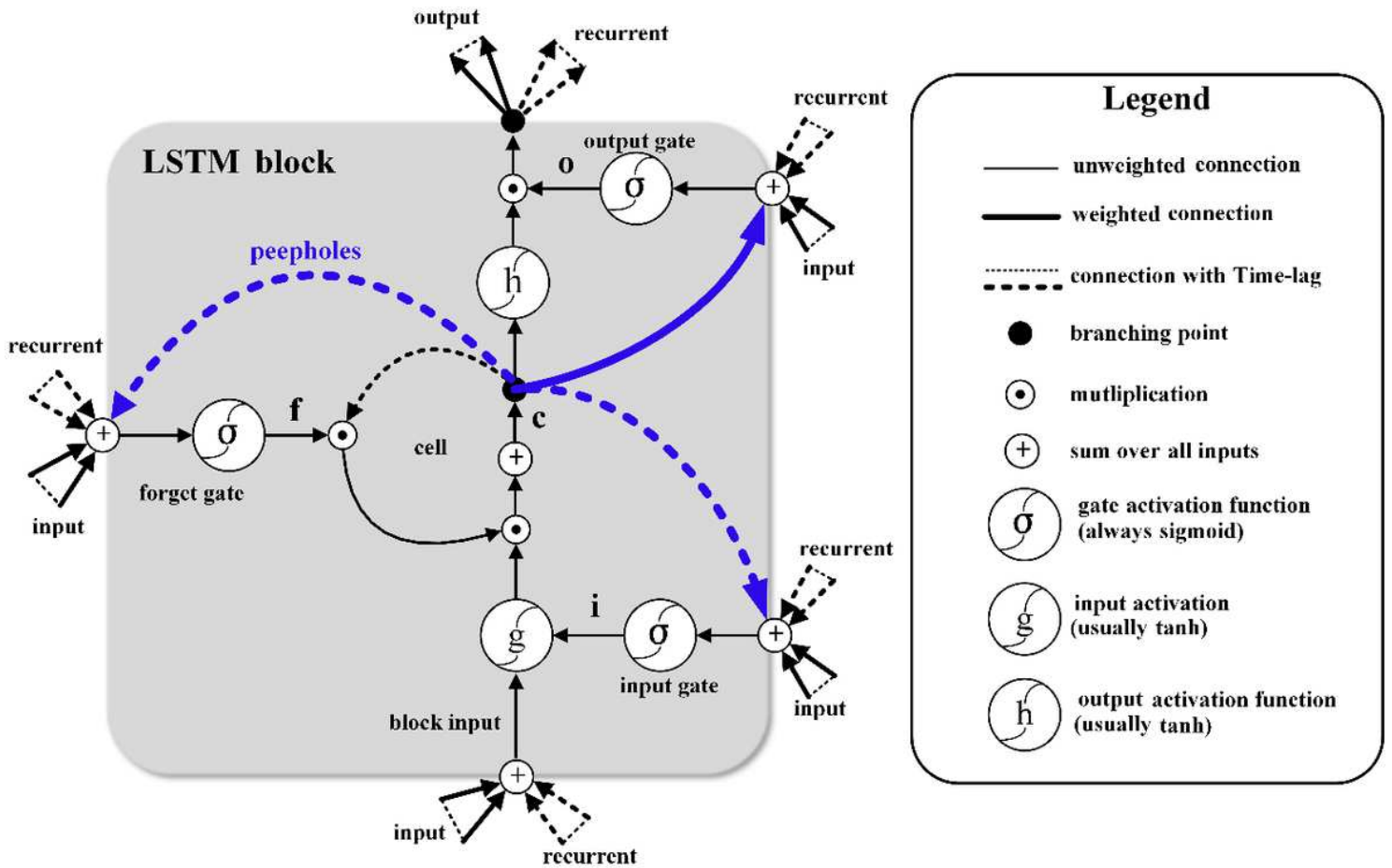


Figure 3

LSTM cell structure in hidden layer.

Hybrid ARIMA-LSTM Model

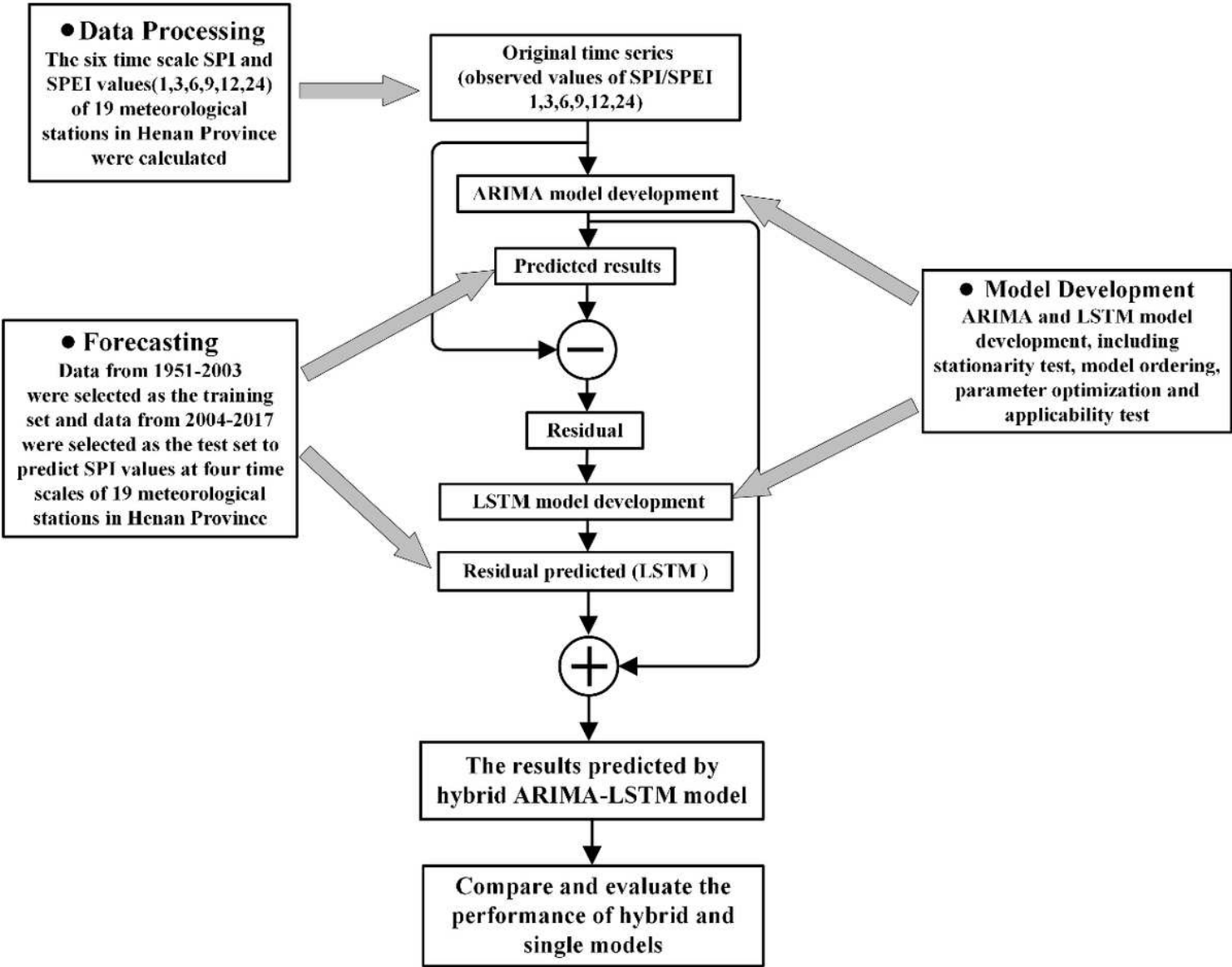


Figure 4

hybrid ARIMA-LSTM model flow chart.

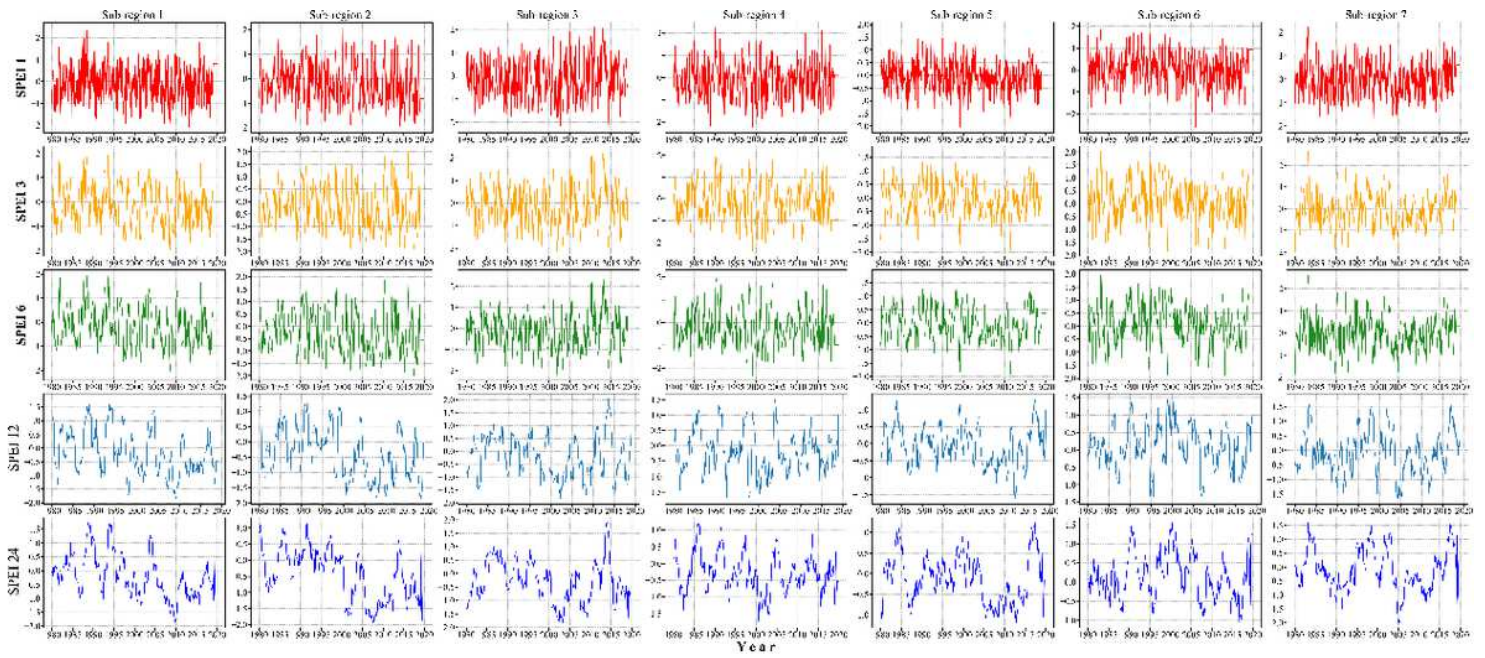


Figure 5

The variations of SPEI at the 1-, 3-, 6-, 12- and 24-month timescales over 1980–2013 in 7 sub-regions of China.

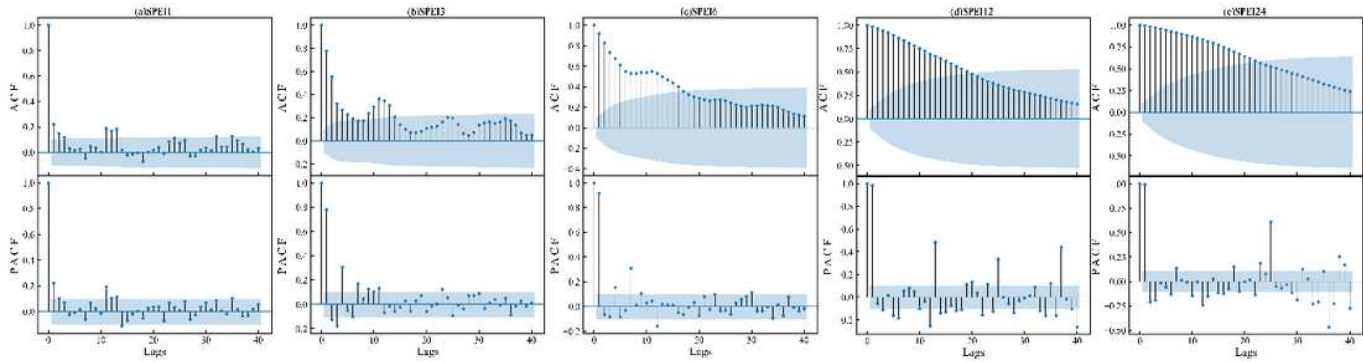


Figure 6

ACF and PACF of SPEI at the 1-, 3-, 6-, 12- and 24-month timescales in sub-region 1 of China.

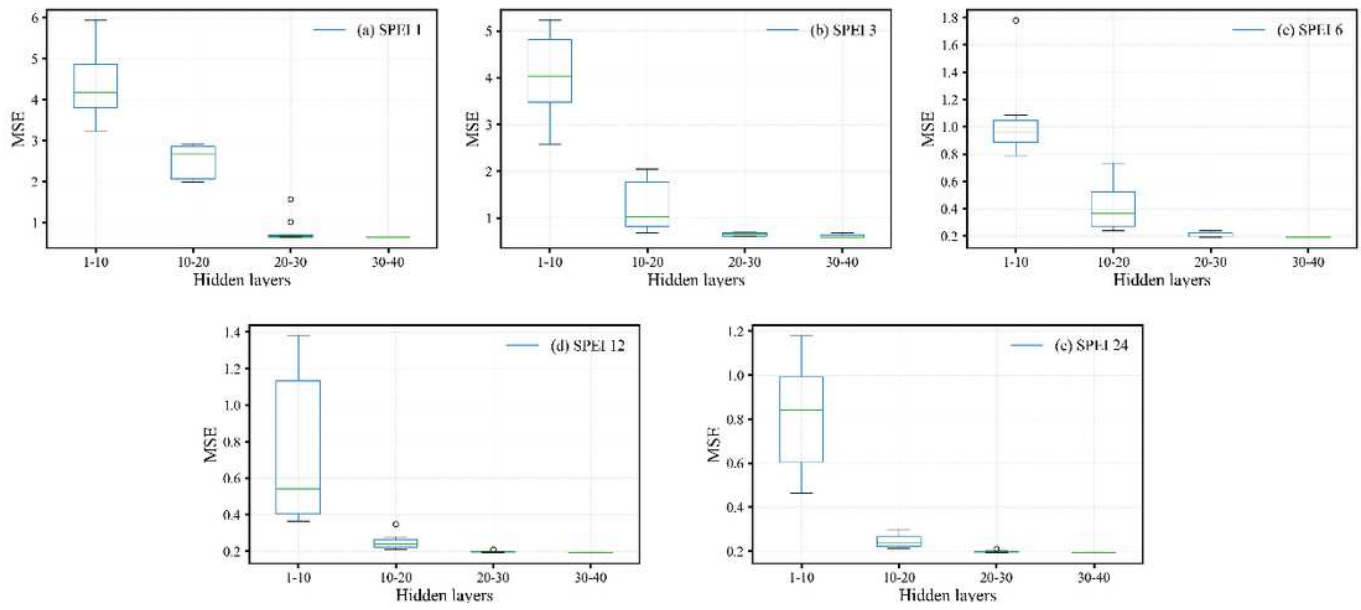


Figure 7

Multitime scale boxplot of loss function and hidden layers of SPEI in sub-region 1 of China.

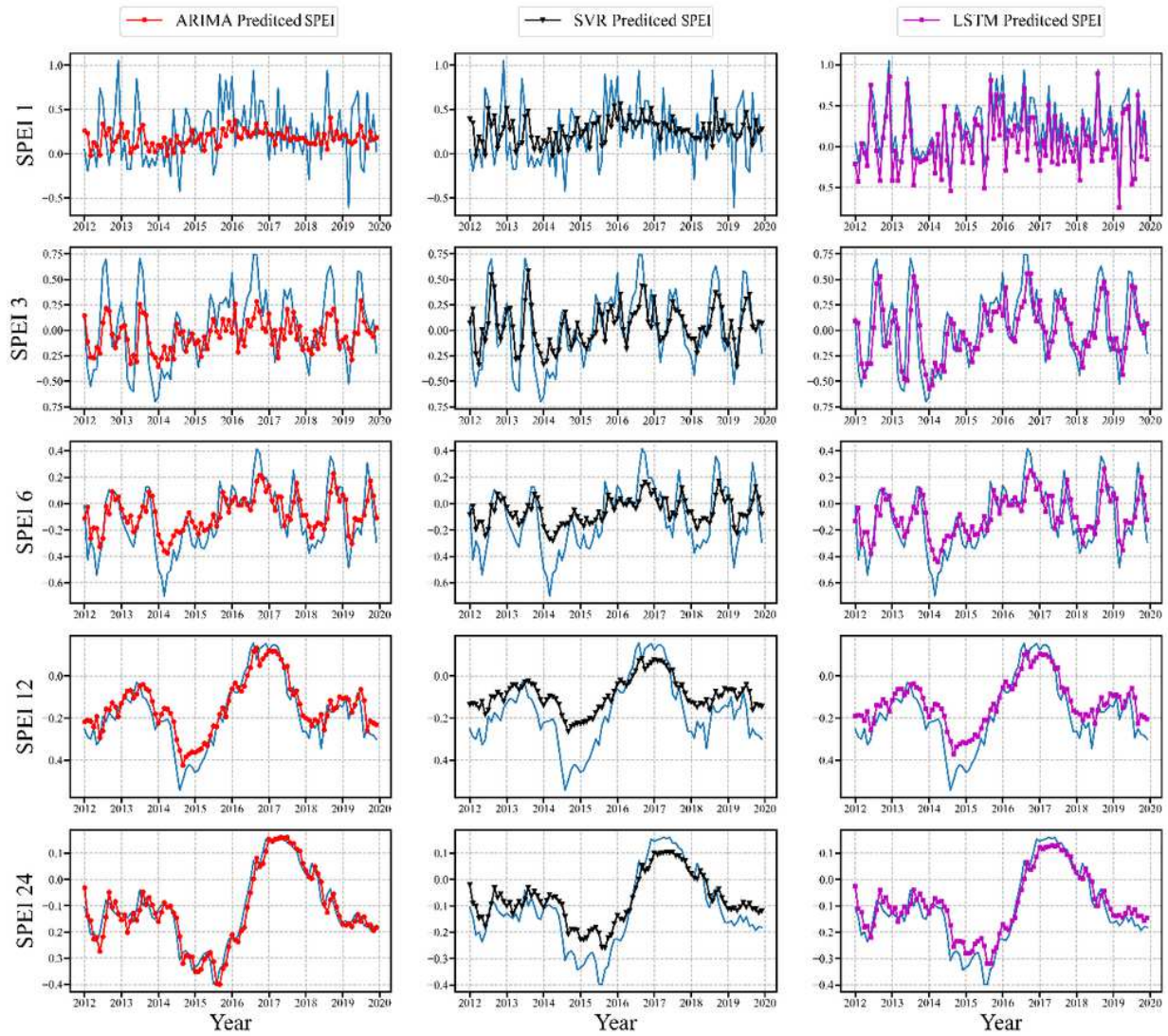


Figure 8

Forecast of multitime scale SPEI value of ARIMA model, SVR model and LSTM model.

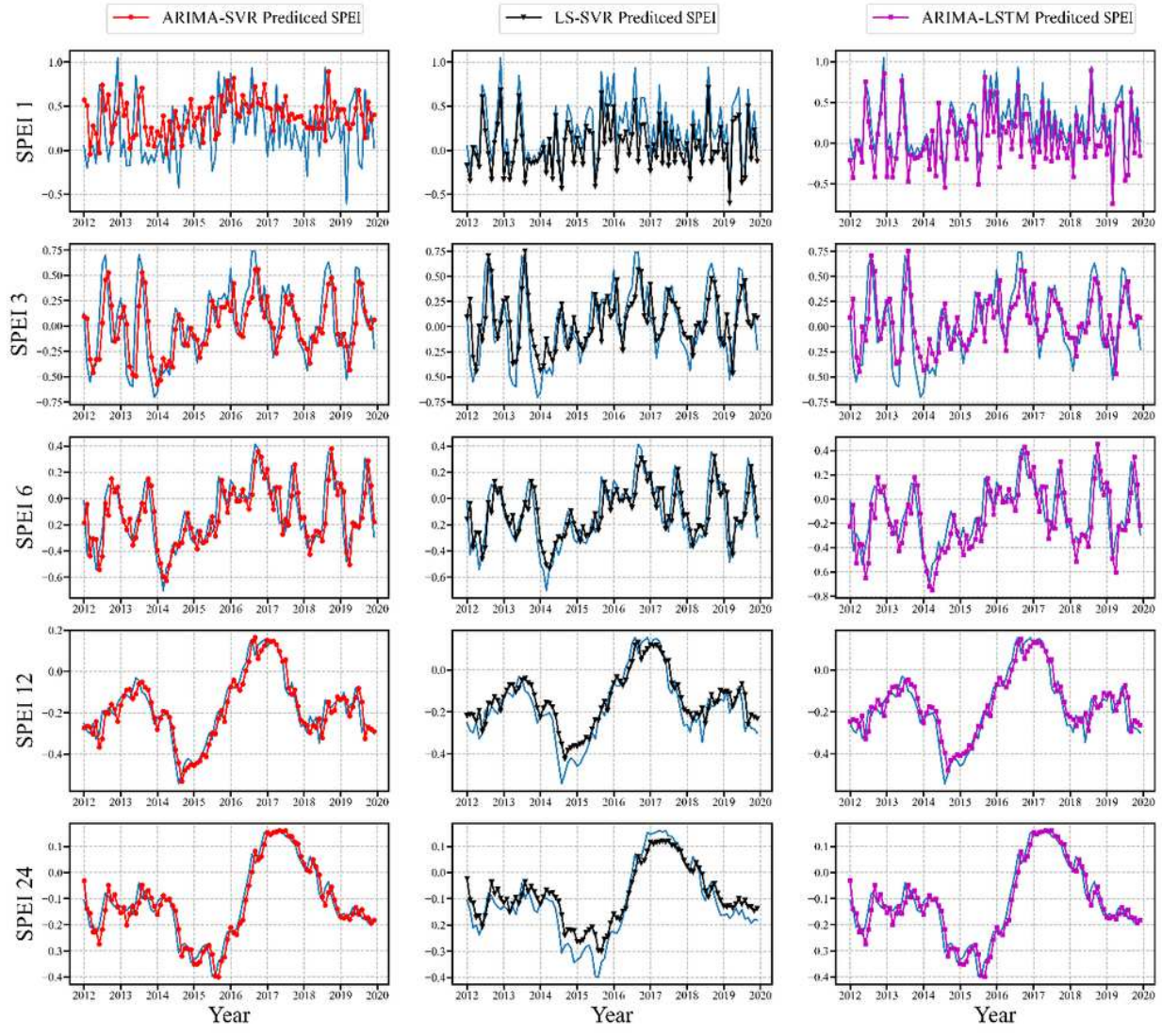


Figure 9

Forecast of multitime scale SPEI value of hybrid ARIMA-SVR model, LS-SVR model and ARIMA-LSTM model.

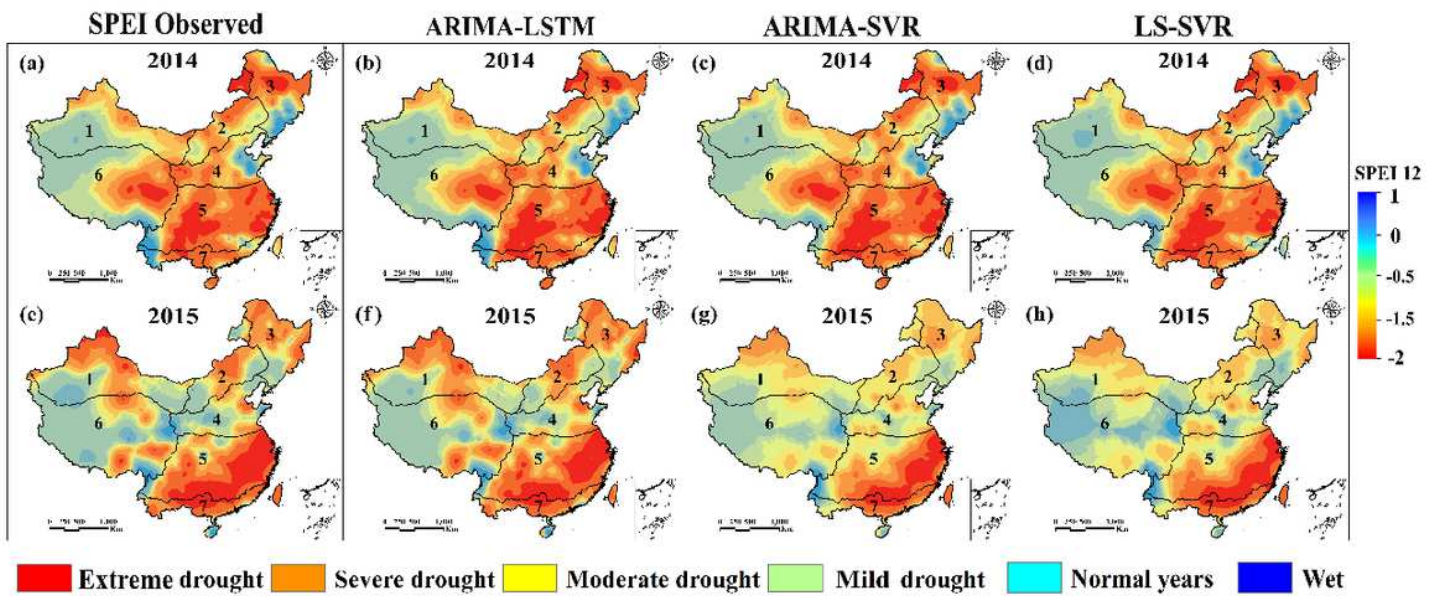


Figure 10

Spatial distributions of SPEI drought levels in 2014 and 2015, using the three forecasting models (ARIMA-SVR, LS-SVR and ARIMA-LSTM model). Note: The designations employed and the presentation of the material on this map do not imply the expression of any opinion whatsoever on the part of Research Square concerning the legal status of any country, territory, city or area or of its authorities, or concerning the delimitation of its frontiers or boundaries. This map has been provided by the authors.